The Astrophysical Journal, 667:780–812, 2007 October 1

BULGES AND DISKLIKE COMPONENTS IN THE HOST GALAXIES OF LOW-REDSHIFT 3CR SOURCES: A NEAR-INFRARED VIEW OF THEIR RADIAL BRIGHTNESS PROFILES[1]

Carlos J. Donzelli,[2,3,4,5] Marco Chiaberge,[3,6] F. Duccio Macchetto,[3,7]
Juan P. Madrid,[3] Alessandro Capetti,[8] and Danilo Marchesini[9]
Received 2006 December 18; accepted 2007 June 7

ABSTRACT

We analyze the near-infrared luminosity profiles and photometric parameters of the host galaxies of 3CR radio sources with $z < 0.3$, to investigate their physical nature. Our sample includes 82 galaxies, of which 22 (27%) are FR Is and 60 (73%) are FR IIs. Using near-infrared data taken both with NICMOS on board the *Hubble Space Telescope* and from the ground with the Telescopio Nazionale Galileo, we find that luminosity profiles are very well described by a single Sérsic law in 52% of the cases and that for the remaining objects (48%) it is necessary to include an exponential profile, which indicates the presence of a second disklike component. The average bulge–to–disklike components luminosity ratio for the galaxies is $(b/e) \sim 1.1$. The analysis of the photometric parameters of the subsamples indicates that FR Is and FR IIs show rather similar bulges in terms of effective surface magnitude, effective radius, and Sérsic index. On the other hand, the disklike components in FR I and FR II hosts show, on average, different properties. Central surface magnitudes are dimmer and scale lengths are greater by a factor of 2 in FR Is when compared to FR IIs. We also estimate the black hole mass associated with each galaxy using two different methods that claim tight correlations of the black hole mass ($M_{\rm BH}$) with the infrared bulge luminosity ($L_{\rm bulge}$) and with the Sérsic index (n). Our data indicate that masses obtained through these two methods show a high dispersion and that $M_{\rm BH}$ obtained through $L_{\rm bulge}$ are systematically higher (by a factor of $\sim$3) than those obtained using n. This result may reflect the fact that for our sample galaxies we do not find any correlation between $L_{\rm bulge}$ and n.

Subject headings: galaxies: active — galaxies: elliptical and lenticular, cD — galaxies: jets — infrared: galaxies — surveys

1. INTRODUCTION

Radio galaxies are a peculiar set of galaxies that give rise to a number of questions regarding their nature: What kind of effects turn these galaxies into radio galaxies? Are these effects related to galaxy morphology or galaxy environment? What are the relations between the properties of radio galaxies and the normal galaxy population? Are these properties a result of the radio activity, or vice versa? In the framework of the AGN unification scheme (Urry & Padovani 1995), radio galaxies are associated with quasars. Therefore the study of such objects plays an important role in constraining physical models of quasar evolution (Kauffmann & Haehnelt 2000), in further testing the unified models, and in exploring the origin of radio loudness (Blandford 2000).

Radio galaxies are usually classified into two morphological classes, edge-darkened FR Is and edge-brightened FR IIs (Fanaroff & Riley 1974), and this dichotomy corresponds to a (continuous) transition in radio power, which occurs at $L_{178} \sim 2 \times 10^{26}$ W Hz^{-1}, with FR Is being the low-power objects. In modern high-resolution radio maps, FR Is are characterized by bright jets near the radio "core" (centered on the host galaxy nucleus), while FR IIs have faint jets (mostly one-sided as a result of relativistic beaming effects) coupled with bright hot spots in the lobes, which mark the location where the jet impacts the ISM.

Optical studies of low-redshift radio galaxies have shown that radio galaxies of both classes are almost invariably associated with giant ellipticals, are generally found in regions of enhanced galaxy density such as clusters or dense groups, and often show signs of interaction (e.g., Zirbel 1997; Gonzalez-Serrano et al. 1993). However, some differences between FR Is and FR IIs seem to be present. The most striking difference is related to the emission-line properties of the two classes: while most (if not all) FR Is only show weak (narrow) emission lines, FR IIs can be distinguished into different subclasses, according to their spectral properties (e.g., Laing 1994). In particular, the role of a subclass of low-excitation FR IIs (LEGs) has still to be fully established: the central engine and environment of LEGs appears very similar to that of FR Is (e.g., Chiaberge et al. 2002; Hardcastle & Worrall 2000), while the radio power and morphology are typical of FR IIs.

While the above topics are the subject of a number of papers, there are very few detailed studies on the photometric properties of the host galaxies of radio galaxies. Zirbel (1996a) analyzes the surface brightness profiles of the host galaxies of low-redshift powerful radio galaxies. This work suggests that FR Is exhibit a weak correlation between the size of the host galaxy and the radio power, and also leads to the conclusion that FR Is and FR IIs inhabit different populations of host galaxies. More specifically, while FR Is are typically associated with cD galaxies, FR IIs are mostly associated with a subclass of ellipticals called "N galaxies." In ground-based images, N-class galaxies appear to have peaked radial brightness profiles, while in *HST* images it is clear that their

[1] Based on observations made with the NASA/ESA *Hubble Space Telescope* (*HST*), obtained at the Space Telescope Science Institute, which is operated by the Association of Universities for Research in Astronomy, Inc., under NASA contract NAS5-26555.

[2] AURA US Gemini Fellow.
[3] Space Telescope Science Institute, 3700 San Martin Drive, Baltimore, MD 21218.
[4] IATE, Observatorio Astronómico, UNC, Laprida 854, Córdoba, Argentina.
[5] CONICET, Rivadavia 1917, Buenos Aires, Argentina.
[6] On leave from INAF, Instituto di Radioastronomia, Via P. Gobetti 101, 40126 Bologna, Italy.
[7] Research and Space Science Department, European Space Agency, ESTEC, Noordwijk, Netherlands.
[8] INAF-Osservatorio Astronomico di Torino, Strada Osservatorio 20, 10025 Pino Torinese, Italy.
[9] Department of Astronomy, Yale University, New Haven, CT 06520.

peculiar profiles are explained by the presence of a bright quasar-like nucleus surrounded by a faint fuzz. Therefore, when deriving the host galaxy profiles, ground-based images are unreliable if a powerful nuclear source is present.

From an imaging study of a sample of radio-quiet quasars, radio-loud quasars, and radio galaxies, Dunlop et al. (2003) conclude that spheroidal hosts become more prevalent with increasing nuclear luminosity. For nuclear luminosities $M_v < -23.5$, the hosts of both radio-loud and radio-quiet quasars are all massive ellipticals. They also suggest that the basic properties of quasar and radio galaxy hosts are indistinguishable from those of quiescent, evolved, low-redshift ellipticals of comparable mass.

The aim of this paper is to provide valuable infrared photometric data of a sample of 82 3CR radio galaxies and to compare these data with those obtained at other wavelengths for both normal and radio galaxies. To achieve this goal we use both ground-based and high angular resolution *HST* data to properly disentangle the host galaxy from any other component related to the AGN. The layout of the paper is as follows. In § 2 we summarize the sample selection and in § 3 we give details on the observations, image reduction, and point-spread function determination. In § 4 we present the galaxy luminosity profiles and profile fitting. In § 5 we discuss the results and in § 6 we analyze these results from the point of view of a different classification of the galaxies of the sample. In § 7 the black hole mass obtained through two different methods is discussed. Finally, in § 8 we summarize our conclusions.

2. SAMPLE SELECTION

The sample of galaxies we analyze belongs to the Revised Third Cambridge Catalogue (3CR; Bennet 1962a, 1962b). The 3CR catalog (Spinrad et al. 1985) is selected at 178 MHz, includes the brightest radio sources in the northern sky ($S_{178} > 10$ Jy), and contains radio galaxies and quasars out to redshifts of $\sim$2. Since this catalog is selected based only on the low-frequency radio properties of the sources, it is an excellent database to study the morphology and photometric attributes of the objects without any orientation bias. We chose all 3CR sources with $z < 0.3$ with the primary goal of characterizing the radio galaxy hosts mostly free from the effects of dust. There is a total of 116 sources in the 3CR up to a redshift of 0.3, and we present here the photometric properties of 82 objects. These objects were randomly observed as part of *HST* snapshot program 10173. Only seven galaxies of the sample were observed as part of other programs. They are 3C 84 (P 7330), 3C 264 (P 7882), 3C 293 (P 9726), 3C 305 (P 7853), 3C 317 (P 7886), 3C 338 (P 7453), and 3C 405 (P 7258). Table 1 lists the observed galaxies together with the observation date, right ascension and declination for epoch J2000.0, FR class (Fanaroff & Riley 1974), and morphological classification.

We used the morphological classification from NED (NASA/IPAC Extragalactic Database) and Zirbel (1996b). As can be noted from Table 1 many of the host galaxies (57%) still remain morphologically unclassified. Most of the galaxies for which a classification is available in the literature are ellipticals. Thirty-four (72%) out of the 47 morphologically classified galaxies are reported as ellipticals, while seven (15%) objects are classified as early spirals and six (13%) as N-type galaxies.

3. OBSERVATIONS AND DATA PROCESSING

We use two different sets of near-infrared data: *HST* NICMOS and Telescopio Nazionale Galileo (TNG) data. *HST* data are essential to derive the radial brightness profile of galaxies located at $z > 0.1$, and particularly for those with a bright nucleus that outshines the host galaxy stellar emission. TNG images are crucial for nearby galaxies ($z < 0.1$), which in general are much larger than the NIC2 field of view and for which a direct measure of the background level is not feasible with the *HST* data alone. In the following we give a brief description of the data sets and the data analysis procedures.

3.1. *HST Observations*

All objects in our sample were observed with NICMOS Camera 2 (NIC2), which has a field of view of $19.2'' \times 19.2''$ and a projected pixel size of $0.075''$. All images were obtained using the F160W filter (similar to the standard *H* band; see Dickinson et al. 2002) and have the same total exposure time of 1152 s. For only a few exceptions exposure times were shorter. These are 3C 84, 3C 264, and 3C 317, for which exposure times were 640, 448, and 640 s, respectively. A more detailed technical description of the observations can be found in Madrid et al. (2006).

We obtained the *HST* NICMOS data from the Multimission Archive at the STScI (MAST). The data was processed by standard OTFR (on-the-fly reprocessing) calibration pipeline. We performed two corrections subsequent to the calibration pipeline: the removal of the pedestal effect and the masking of the coronagraphic spot. Bad columns and bad pixels were masked out too. The pedestal effect is stochastic noise introduced during the detector readout (Noll et al. 2004). Each of the quadrants of the detector has a different offset. One in particular appears darker when compared to the others. We remove this effect using the IRAF task `pedsub`, in the Space Telescope Science Analysis System (STSDAS). NIC2 has a hole to allow coronagraphic observations; this hole produces a spot on our images and therefore we mask this spot before image combination. Information is recovered using the four-dither pattern used for the observations. We combine the four exposures using the Pyraf task `multidrizzle`, also in STSDAS (Koekemoer et al. 2002). The final image is the output of `multidrizzle`, in units of e^- s^{-1}. During our data reduction we preserve both the original sky level and the original pixel size of $0.075''$.

For the photometric calibration of the reduced data we used the formula of Dickinson et al. (2002) to derive a Vega-normalized magnitude for F160W (NIC2). We then have $m(\mathrm{F160W}) = -2.5 \log [\mathrm{PHOTFNU} \times \mathrm{CR}/f_\nu(\mathrm{Vega})] = 22.107 - 2.5 \log (\mathrm{CR})$, where PHOTFNU = 1.49816×10^{-6} Jy s DN^{-1}, and CR is the count rate in DN s^{-1}. The flux density of Vega in the F160W band for NIC2 is $f_\nu(\mathrm{Vega}) = 1043.5$ Jy. These magnitude units are different from the ST instrumental magnitudes used by Madrid et al. (2006). We chose the Vega system because it is more similar to the standard ground-based near-IR system, and for the F160W filter the difference between Vega magnitude and ST magnitude corresponds to 3.68 mag.

A visual inspection of our final images revealed that the amplifier-glow-effect residuals were not negligible. The amplifier glow is caused by the readout amplifier situated close to each corner of the detector, and even after the correction was applied we noted that residuals for most cases were around 10%–20% above the background level. We trim the border of the images to obtain accurate surface photometry and eliminate the amplifier glow. The resulting final field of view is $16.5'' \times 16.5''$.

3.2. *TNG Data*

We have used the images taken by Marchesini et al. (2005). These images were obtained with the 3.6 m Telescopio Nazionale Galileo (TNG), the Italian national facility located on the island of La Palma (Spain). These observations were made in two runs on 2000 July 8–12 and 2001 February 9–13. ARNICA (ARcetri Near Infrared CAmera) was used in the first run and NICS (Near

TABLE 1

OBSERVATION LOG

Source (1)	Date (UT) (2)	α (J2000.0) (3)	δ (J2000.0) (4)	FR Class (5)	Morphological Class (6)
3C 17	2006 Jul 2	00 38 20.5	−02 07 41.0	II (QSO)	E pec
3C 20	2005 Feb 27	00 43 09.27	+52 03 36.66	II (HEG)	...
3C 28	2005 Jun 13	00 55 50.65	+26 24 36.93	II (LEG)	E
3C 31*	2005 Jun 17	01 07 24.99	+32 24 45.02	I	BCG; SA0−
3C 33.1	2004 Aug 15	01 09 44.27	+73 11 57.2	II (QSO)	...
3C 35*	2005 Mar 16	01 12 02.29	+49 28 35.33	II (LEG)	...
3C 52	2005 Mar 11	01 48 28.90	+53 32 27.9	II (LEG)	...
3C 61.1	2004 Aug 9	02 22 36.00	+86 19 08.0	II (LEG)	...
3C 66B*	2004 Nov 5	02 23 11.46	+42 59 31.34	I	E
3C 75N*	2004 Nov 11	02 57 41.55	+06 01 36.58	I	E0
3C 76.1*	2005 Feb 6	03 03 15.0	+16 26 19.85	I	E1?
3C 79	2004 Oct 30	03 10 00.1	+17 05 58.91	II (QSO)	E
3C 83.1*	2005 Mar 12	03 18 15.8	+41 51 28.0	I	E+
3C 84*	1998 Mar 16	03 19 48	+41 30 42	I	cD pec
3C 88*	2004 Nov 6	03 27 54.17	+02 33 41.82	II (LEG)	E pec?
3C 98*	2005 Nov 25	03 58 54.4	+10 26 03	II (HEG)	E1?
3C 105	2004 Oct 26	04 07 16.46	+03 42 25.68	II (HEG)	E
3C 111*	2004 Dec 8	04 18 21.05	+38 01 35.77	II (QSO)	N
3C 123	2004 Dec 7	04 37 04.4	+29 40 13.2	II (LEG)	...
3C 129*	2004 Dec 8	04 49 09.07	+45 00 39.0	I	E
3C 129.1*	2004 Nov 22	04 50 06.7	+45 03 06.0	I	E
3C 132	2005 Nov 24	04 56 43.0	+22 49 22	II (LEG)	...
3C 133	2004 Dec 13	05 02 58.4	+25 16 28.0	II (LEG)	...
3C 135	2005 Apr 8	05 14 08.3	+00 56 32.0	II (HEG)	E
3C 153	2005 Nov 25	06 09 32.5	+48 04 15	II (LEG)	...
3C 165	2005 Apr 26	06 43 06.6	+23 19 03.0	II (LEG)	...
3C 166	2005 Nov 4	06 45 24.1	+21 21 51	II (LEG)	E
3C 171	2004 Nov 14	06 55 14.72	+54 08 58.27	II (HEG)	N
3C 173.1	2004 Nov 22	07 09 24.34	+74 49 15.19	II (LEG)	...
3C 180	2005 Feb 20	07 27 04.77	−02 04 30.97	II (LEG)	...
3C 184.1	2004 Nov 26	07 43 01.28	+80 26 26.3	II (QSO)	E
3C 192*	2005 Jan 8	08 05 35.0	+24 09 50.0	II (HEG)	...
3C 196.1	2005 Feb 1	08 15 27.73	−03 08 26.99	II (QSO)	cD
3C 197.1	2005 Apr 19	08 21 33.7	+47 02 37.0	II (HEG)	...
3C 198	2005 May 3	08 22 31.9	+05 57 7.0	II (HEG)	E
3C 213.1	2005 Feb 12	09 01 05.3	+29 01 46.0	II (LEG)	...
3C 219	2004 Sep 14	09 21 08.64	+45 38 56.49	II (QSO)	...
3C 223	2005 Feb 10	09 39 52.76	+35 53 59.12	II (QSO)	E2
3C 223.1	2005 Jan 18	09 41 24.04	+39 44 42.39	II (HEG)	S0?
3C 227	2005 Mar 28	09 47 45.14	+07 25 20.33	II (QSO)	N
3C 234	2005 Nov 3	10 01 49.5	+28 47 09	II (QSO)	N
3C 236*	2004 Nov 2	10 06 01.7	+34 54 10.0	II (LEG)	E
3C 264*	1998 May 12	11 45 05.0	+19 36 23	I	E
3C 277.3*	2005 Mar 24	12 54 12.06	+27 37 32.66	II	E
3C 284	2006 Mar 4	13 11 04.7	+27 28 08	II (HEG)	...
3C 285	2004 Dec 5	13 21 17.8	+42 35 15.0	II (HEG)	...
3C 287.1	2005 Jul 16	13 32 53.27	+02 00 44.73	II (QSO)	E pec
3C 288	2004 Oct 31	13 38 50.0	+38 51 10.7	I	...
3C 293*	2004 Mar 17	13 52 17.8	+31 26 46	II (LEG)	...
3C 296*	2006 Apr 21	14 16 52.9	+10 48 26	I	...
3C 300	2006 Mar 4	14 23 01.0	+19 35 17	II (HEG)	E
3C 303	2004 Dec 26	14 43 02.74	+52 01 37.5	II (QSO)	N
3C 305*	1998 Jul 19	14 49 21.6	+63 16 14	I	SB0
3C 310*	2004 Aug 13	15 04 57.18	+26 00 56.87	I	...
3C 314.1	2005 Feb 24	15 10 23.12	+70 45 53.4	I	E
3C 315	2004 Dec 30	15 13 40.0	+26 07 27.0	I	...
3C 317*	1998 Aug 26	15 16 44.5	+07 01 17	I	cD; E
3C 319	2004 Dec 29	15 24 05.5	+54 28 14.6	II (LEG)	...
3C 326	2006 Apr 21	15 52 09.1	+20 05 24	II (LEG)	...
3C 332	2006 Jan 12	16 17 42.5	+32 22 35	II (QSO)	E
3C 338*	1997 Dec 17	16 28 38.5	+39 33 06	I	...
3C 346	2005 May 19	16 43 48.69	+17 15 48.09	II (LEG)	E
3C 348	2005 May 9	16 51 08.16	+04 59 33.84	I	E

TABLE 1—*Continued*

Source (1)	Date (UT) (2)	α (J2000.0) (3)	δ (J2000.0) (4)	FR Class (5)	Morphological Class (6)
3C 349	2005 Mar 23	16 59 28.84	+47 02 56.8	II (HEG)	...
3C 353*	2004 Sep 9	17 20 28.16	−00 58 47.06	II (LEG)	SA0–
3C 357	2006 Mar 25	17 28 18.5	+31 46 14	II (HEG)	E
3C 379.1	2004 Nov 5	18 24 32.53	+74 20 58.64	II (HEG)	...
3C 381	2004 Nov 11	18 33 46.29	+47 27 02.9	II (HEG)	...
3C 386*	2005 Jun 15	18 38 26.27	+17 11 49.57	I	SA0–
3C 388*	2004 Oct 19	18 44 02.4	+45 33 30.0	II (LEG)	...
3C 401	2004 Aug 11	19 40 25.14	+60 41 36.85	II (LEG)	E
3C 402*	2004 Dec 10	19 41 46.0	+50 35 44.9	II (HEG)	S?
3C 403*	2004 Nov 6	19 52 15.81	+02 30 24.4	II (HEG)	S0
3C 405*	1997 Dec 16	19 59 28.3	+40 44 02	II (HEG)	S?
3C 424	2006 Jun 22	20 48 12.0	+07 01 17.0	I	E
3C 433	2004 Aug 18	21 23 44.6	+25 04 28.5	II (HEG)	...
3C 436	2004 Nov 9	21 44 11.74	+28 10 18.67	II (HEG)	...
3C 438	2004 Nov 18	21 55 52.3	+38 00 30.0	II (HEG)	...
3C 449*	2004 Nov 11	22 31 20.63	+39 21 30.07	I	...
3C 452	2004 Nov 28	22 45 48.9	+39 41 14.47	II (HEG)	E
3C 459	2006 Jun 24	23 16 35.2	+04 05 18.0	II (LEG)	N
3C 465*	2004 Sep 28	23 38 29.41	+27 01 53.03	I	cD; E+ pec

NOTES.—Col. (1): 3CR number (an asterisk indicates that the galaxy was also observed with TNG). Col. (2): *HST* observation date. Cols. (3)–(4): Right ascension and declination. Units of right ascension are hours, minutes, and seconds, and units of declination are degrees, arcminutes, and arcseconds. Col. (5): FR class. Col. (6): Morphological classification.

Infrared Camera Spectrometer) was used in the second run. ARNICA uses a 256×256 pixel^2 NICMOS 3 array with a pixel size of $0.35''$ and a total field of view (FoV) of $1.5' \times 1.5'$, which is more than 5 times greater than the FoV of the *HST* NIC2. On the other hand, NICS uses a Rockwell 1024×1024 HgCdTe Hawaii array. NICS has two modes available, the small-field mode with a pixel size of $0.13''$ and a FoV of $2.2' \times 2.2'$, and the large-field mode in which the pixel size and FoV are doubled. For both ARNICA and NICS observations the K' filter was used. This filter has a central wavelength of 2.12 μm and a FWHM of 0.35 μm. For NICS total integration times of 20 minutes were used, while for ARNICA total integration times ranged from 5 to 24 minutes, depending on the source. More detailed information about the individual observations is listed in Table 3 of Marchesini et al. (2005).

3.3. *Background Subtraction and PSF Modeling*

Since suitable fitting of radial profiles at low surface brightness levels is a delicate task, we are extremely cautious in the determination of the background level and its uncertainty. First of all, most of the galaxies with $z < 0.1$ cover the whole FoV of *HST* NICMOS, and therefore the background cannot be measured directly. Furthermore, a detailed analysis of the background level for the rest of the galaxies with smaller apparent diameter (those with $z > 0.1$) shows that the background is not constant. In fact, background variations among these images can be as large as 40% or more, which makes it impossible to remove it using a common value for all images. Therefore, each image of the $z > 0.1$ galaxies are to be carefully examined in order to determine the proper background level. However, our analysis shows that, in each image, a constant value across the whole detector's FoV is accurate enough to remove the background. For those images where this task was possible, background removal left residuals not higher than 5%.

For galaxies with $z < 0.1$ the approach is completely different. Since we are not able to determine the background on NICMOS images given that these galaxies cover the whole chip, we use ground-based K'-band images taken with the TNG. Because of the much larger FoV, these images allow us to easily determine the sky level and also to obtain accurate luminosity profiles in the external regions of the galaxies. The next step is to simply determine the adequate offset in order to match the luminosity profiles obtained from the TNG images with those obtained from the *HST*. The matching was done in an intermediate region of the luminosity profiles, avoiding the innermost regions of the TNG profiles, where seeing effects are important, and avoiding the outermost region of the *HST* profiles where background effects are noticeable. We find that zero points needed to match TNG profiles with *HST* profiles are surprisingly constant over the observation dates and that the estimated errors were less that 0.05 mag arcsec^{-2}. This was done assuming the $H - K'$ color gradient is null for our galaxies. This assumption of null color gradient is supported by the fact that we do not detect any $H - K'$ color gradient for the galaxies with $z > 0.1$, where an accurate background determination on both the TNG and *HST* images is possible. Further support for this assumption is found in Möllenhoff & Heidt (2001, hereafter MH01). These authors showed that in a sample of 40 bright spiral galaxies the structural parameters for both the bulge and the disk components are identical for *JHK* filters, within the error they estimate from the data.

PSF modeling for NIC2 is well described by Suchkov & Krist (1998) and references therein. PSF diffraction structures, such as Airy rings and spikes, grow larger with increasing wavelength and therefore one must be very cautious when using infrared images. In our case, only a few cases show a bright nuclear source that causes bright PSF diffraction patterns on the images. In order to get rid of these patterns we have used the Tiny Tim modeling software (Krist 1993) to create suitable PSF models for each of the selected images. These models were then subtracted from the individual images. This procedure works well in most images; if larger residuals were noticed they were properly masked before any isophote fitting. Besides, during the fitting procedure we also discarded the inner 3 pixels ($0.23''$) of the luminosity profiles we obtained. This was done following the results we obtained by

running a test series as described in Coenda et al. (2005). Basically, these tests consist of generating model images of several galaxies with different photometric parameters. These images were then convolved with the NIC2 PSF prior to the luminosity profile extraction. Finally, we fitted equation (1) to the profiles we obtained in regions of different semimajor axis. This allowed us to determine the minimum radius of the luminosity profile we can use for the fit in order to recover the photometric parameters of the galaxies we model. We conclude that the most suitable region for profile fitting is that for $r > 0.23''$. This is approximately twice the NIC2-PSF FWHM with the F160W filter. With this restriction, the parameters that we obtain have associated errors that are below those calculated in § 4.

4. LUMINOSITY PROFILES AND FITTING FUNCTIONS

There are numerous methods for extracting luminosity profiles. The variety includes one-dimensional analysis (Bagget et al. 1998), ellipse fitting to the isophotes of the galaxies (Héraudeau & Simien 1996), and two-dimensional analysis (Byum & Freeman 1995). At first glance our infrared images show mostly elliptical galaxies with no trace of any further structures, and in a few cases (20%) we can detect dust lanes, jets, or plumes. Therefore, we are mostly working with axisymmetric structures that can be easily analyzed with azimuthal isophote fitting. For this purpose, we use the `ellipse` routine within STSDAS (Jedrzejewski 1987). Before extracting the galaxy profile, we carefully mask all spurious objects such as stars and residual diffraction patterns.

In the case of two galaxies overlapping, once we obtain the luminosity profile and structural parameters (center coordinates, ellipticity, and position angle of the isophotes), we construct a model galaxy using `bmodel` (within STSDAS) that is subtracted from the original image. The resulting image is then used to extract the luminosity profile of the remaining galaxy. This process is repeated several times until the luminosity profiles of both galaxies converge.

Isophote fitting was performed up to a count level of 2 $\sigma_{\rm sky}$; i.e., we stopped the fitting procedure when the isophote level is around twice the background dispersion (pixel-to-pixel variance), which corresponds to a surface magnitude of $\mu_{\rm F160W} = 21.8$ mag arcsec^{-2} on the *HST* NICMOS images. This procedure is used to derive the luminosity profiles from both the TNG and the *HST* images.

4.1. *Profile Fitting*

Similarly to profile extraction, luminosity profile fitting can be done using a wide variety of functions. The most common functions are the classical de Vaucouleurs $R^{1/4}$ profile (de Vaucouleurs 1948), the exponential profile (Freeman 1970), and the most general Sérsic profile R^{β}, where the concentration parameter $\beta = 1/n$ is the inverse of the Sérsic index (Sérsic 1968). Generally, the $R^{1/4}$ profile describes very well the luminosity profile of bulges, while the exponential profile is used to fit the luminosity profile of disks. However, it was recently found that the $R^{1/4}$ function does not describe the bulge profile for many ellipticals correctly. As a result, many authors use the more general R^{β} profile, as is the case for Brown et al. (2003). However, for 45% of our sample galaxies, we find that a single Sérsic profile still cannot fit the data. Therefore, we try a more general case using two Sérsic profiles in order to fit the inner and outer regions of the luminosity profiles respectively. We find that the outer profile regions are well fitted with a concentration index $\beta \sim 1$, equivalent to an exponential disk. This result is similar to that found by Seigar et al. (2007). These authors analyze a sample of five cD galaxies and find that the surface brightness profiles are best fit by an inner Sérsic model with $\beta \sim 1$–0.16 and an outer exponential component. As de Jong et al. (2004) point out, the exponential luminosity profile does not prove that these galaxies have real disks in the usual sense of rotation-supported stellar systems. Kinematic data are required to confirm the presence of a disk in any individual galaxy. Therefore, throughout this paper we refer to this component as a disklike component. The adopted fitting function has only five free parameters and can be written in the following form:

$$I(r) = I_s \exp\left[-k\left(\frac{r}{r_e}\right)^{\beta} - 1\right] + I_0 \exp\left(-\frac{r}{r_0}\right). \quad (1)$$

In this equation the first term corresponds to the Sérsic profile, where I_s is the intensity at $r = 0$ and r_e is the radius that encloses half of the total luminosity of the bulge (also known as the effective radius); k can be calculated using $k \sim 2/\beta - 0.33$. Similarly, $I_e = I_s \exp(-k)$, which is the intensity at $r = r_e$ (MH01). The second term corresponds to the exponential profile, where I_0 is the central intensity and r_0 is the scale length.

The panels of Figure 1 show the luminosity profile for all the galaxies of our sample. In these panels NICMOS data are represented by squares while data from TNG are represented by triangles. The fitting functions are also displayed for the bulge (*short-dashed line*), the disklike component (*long-dashed line*), and the sum of both components (*solid line*). The radius is in kiloparsecs (*bottom horizontal axis*) and arcseconds (*top horizontal axis*).

The parameters described in equation (1) were obtained using the `nfit` routine within STSDAS (Schombert & Bothun 1987). The fitting procedure was carried out only in the S/N > 2 portion of the galaxy surface brightness profiles. This was done to exclude the regions in the faint end of the luminosity profiles, in which the error is large and the information is poor. We also excluded the inner 3 pixels ($\sim 0.20''$) of the luminosity profiles in order to avoid any contamination resulting from the PSF subtraction. The errors on the parameters are calculated following the method described by Coenda et al. (2005). Briefly, this technique consists of creating test images to which we artificially add and subtract a constant value corresponding to $\sigma_{\rm sky}$. We then extract the new luminosity profile as explained above and fit it with equation (1). These newly obtained parameters give us the respective upper and lower limits.

Intensity parameters are then converted into surface brightness, expressed in mag arcsec^{-2} by the equation $m = -2.5 \log I$, while units of r_e and r_0 are converted to kiloparsecs. Measured errors for r_e and r_0 are smaller than 15% while those for μ_e and μ_0 are below 0.20 mag arcsec^{-2}. The total luminosities of both the bulge and the exponential components are finally computed using the derived photometric parameters and integrating separately both terms of equation (1) as follows:

$$L = \int_0^{\infty} I(r) 2\pi r \, dr, \quad (2)$$

which yields

$$L_{\rm bulge} = I_s r_e^2 \pi \frac{2}{\beta k^{2/\beta}} \Gamma(2/\beta) \quad (3)$$

for the bulge component and

$$L_{\rm disklike\ component} = 2\pi I_0 r_0^2 \quad (4)$$

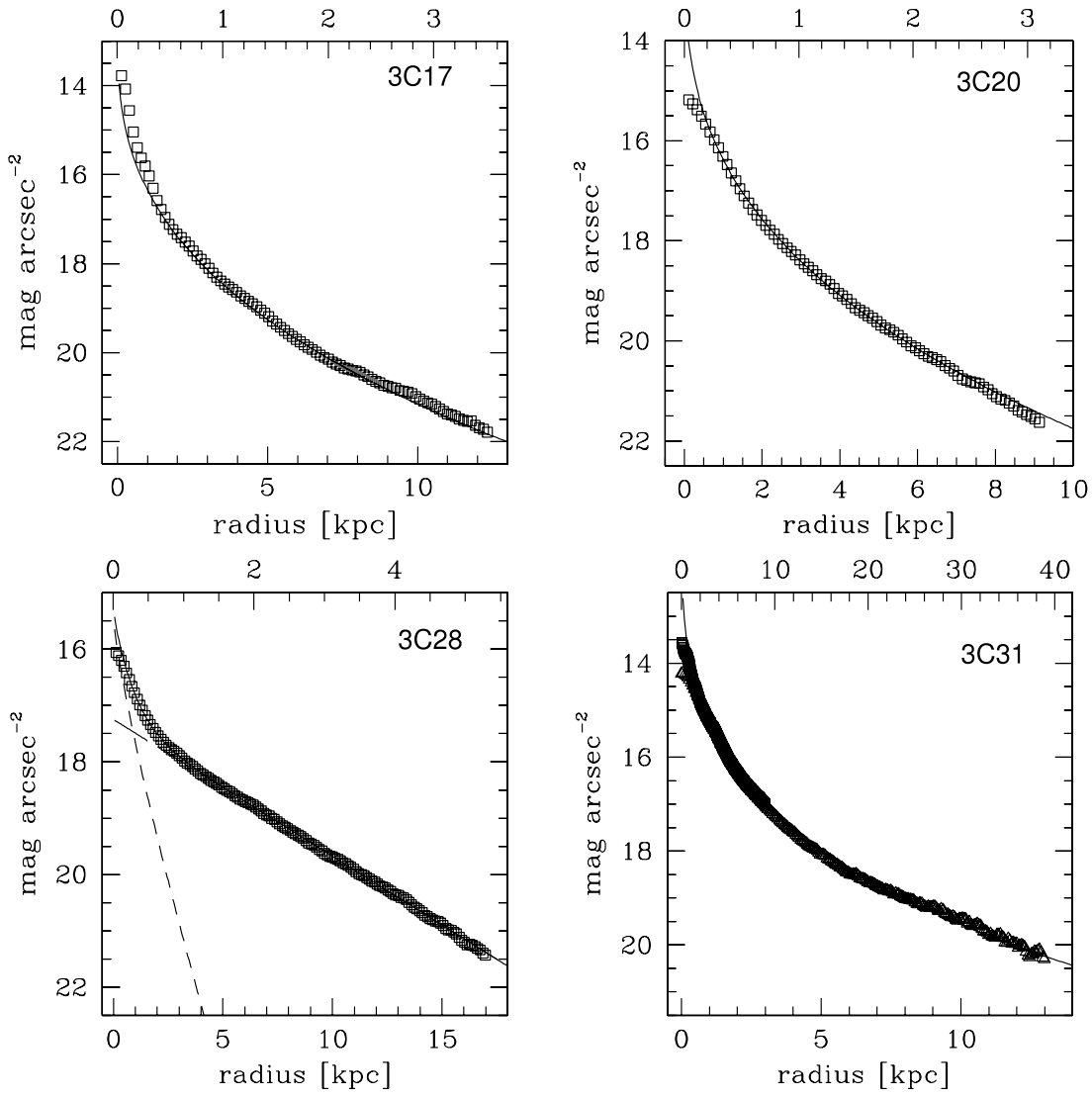

FIG. 1.— Luminosity profiles. Squares represent NICMOS F160W data while triangles represent TNG K' data scaled to the NICMOS filter. Upper ordinates give radius in units of arcseconds. The solid line shows the sum of the bulge (*short-dashed line*) plus disklike component (*long-dashed line*) fitting functions.

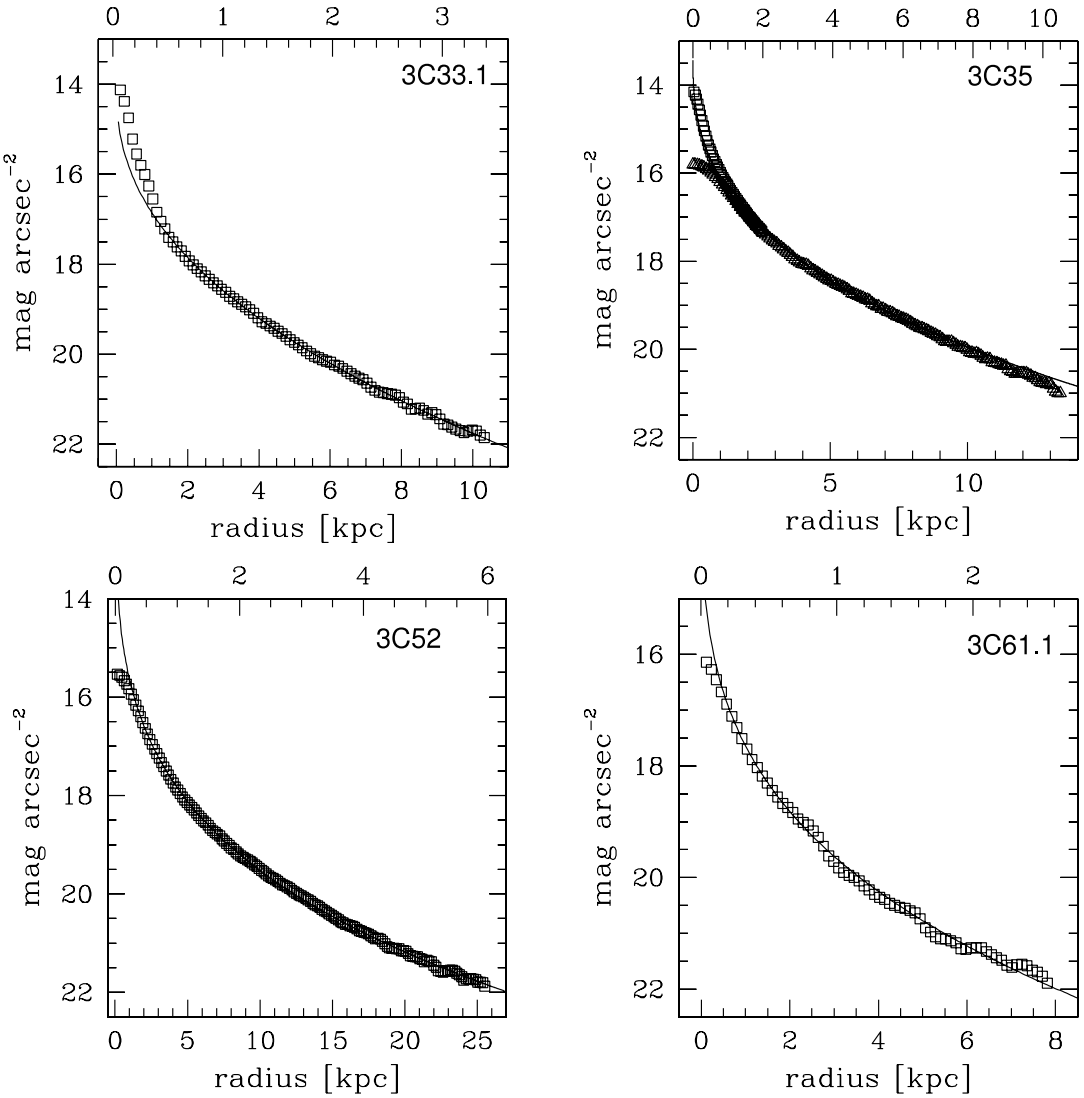

FIG. 1—*Continued*

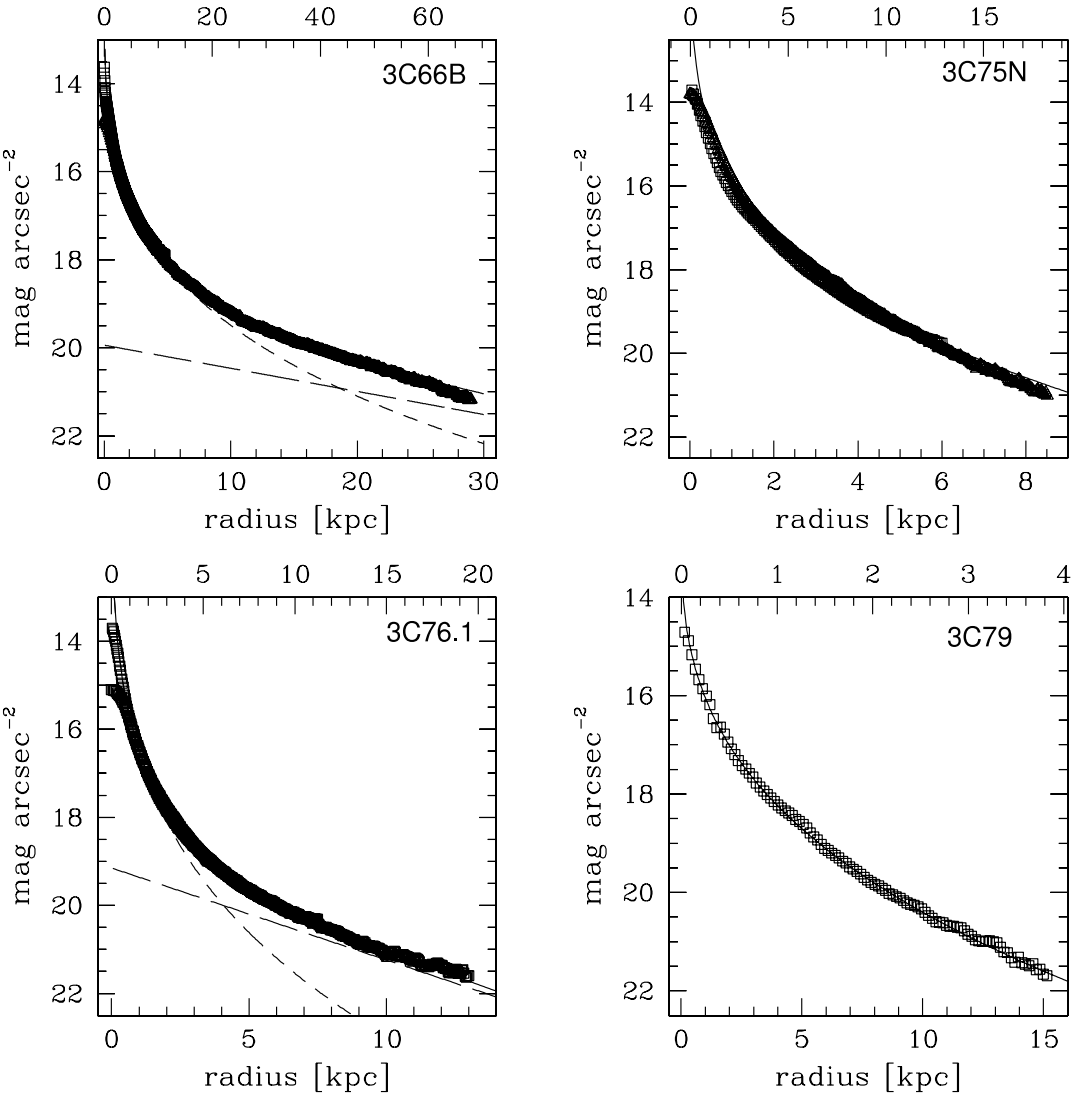

FIG. 1—*Continued*

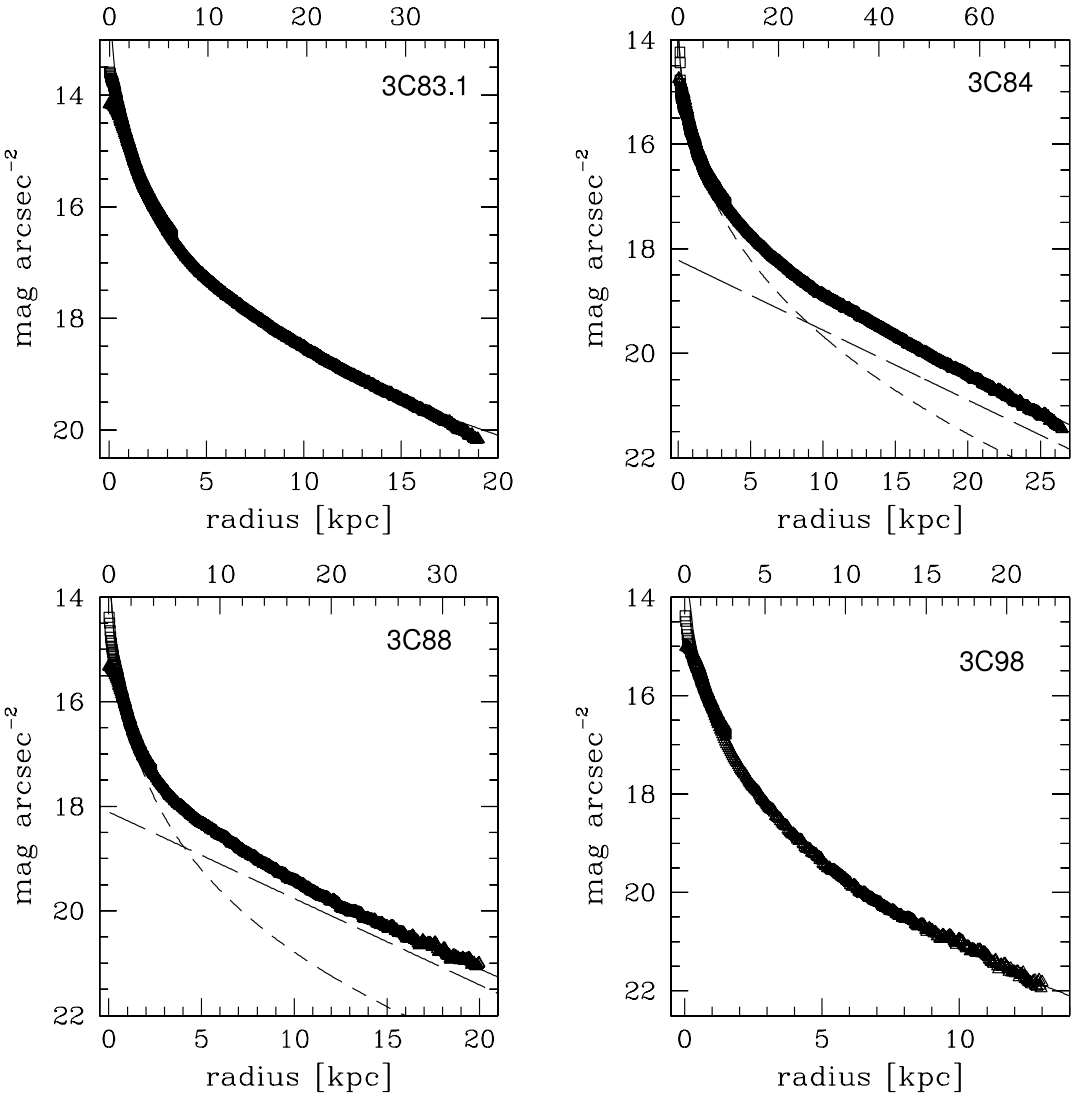

FIG. 1—*Continued*

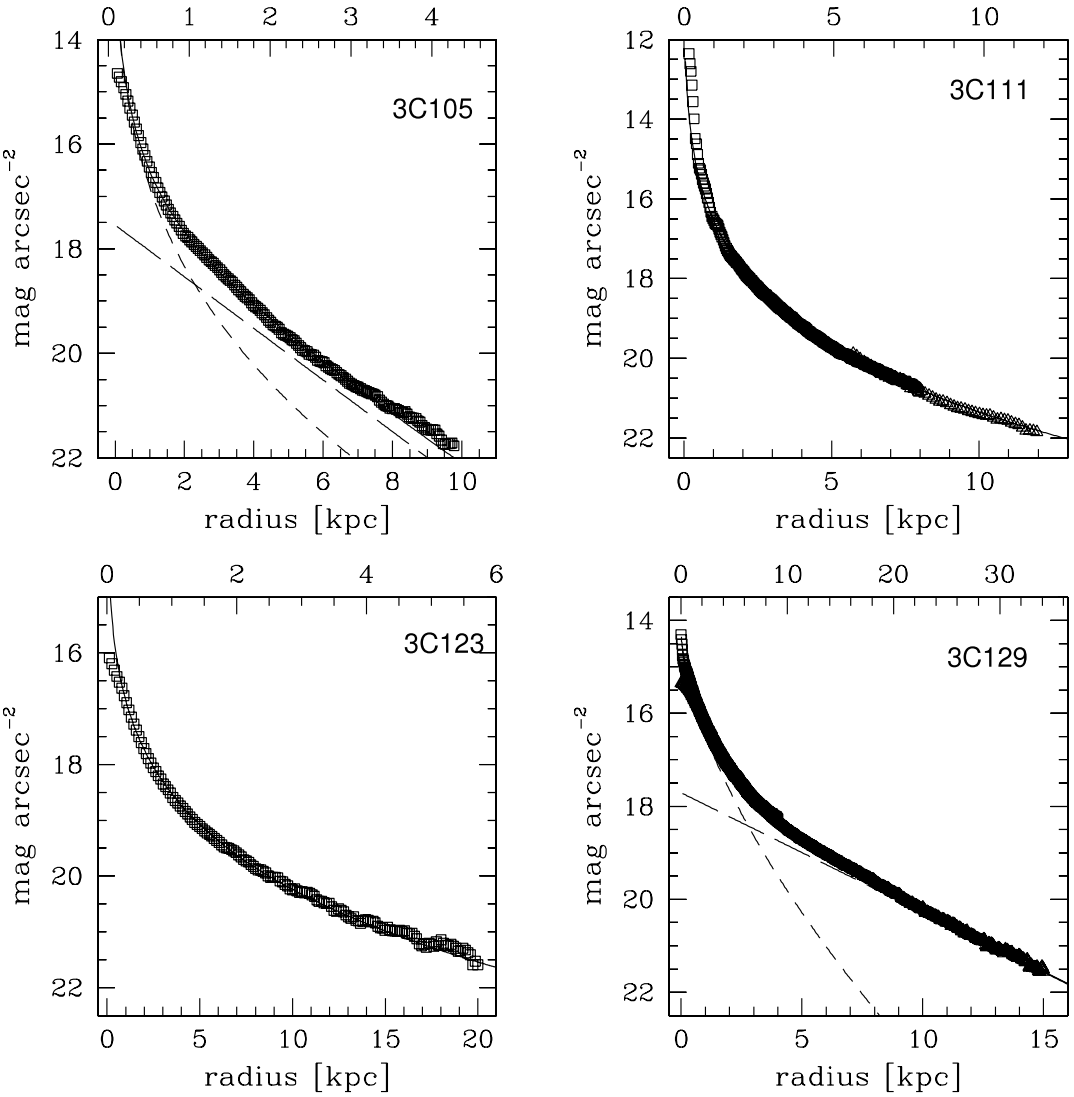

FIG. 1—*Continued*

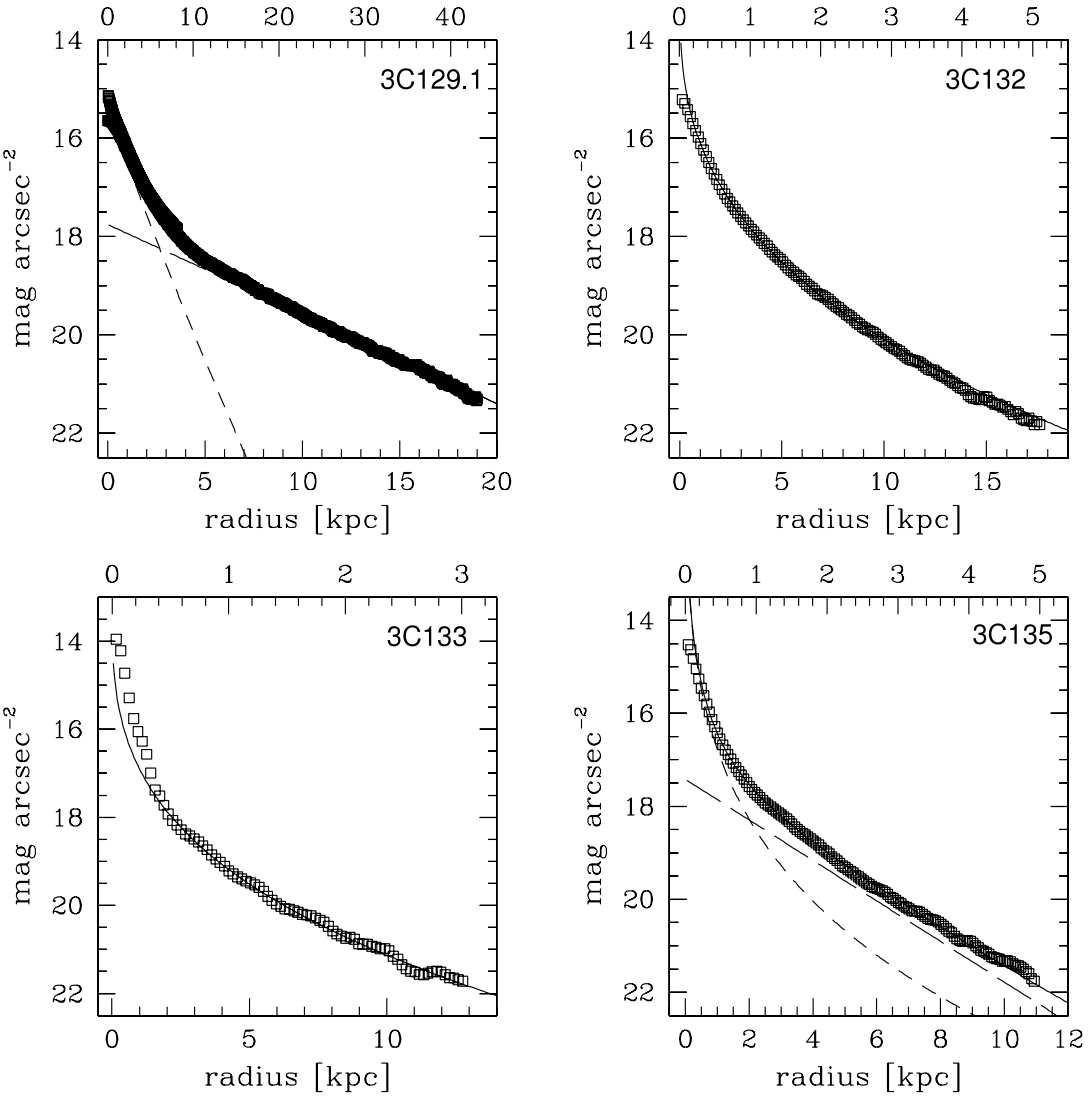

FIG. 1—*Continued*

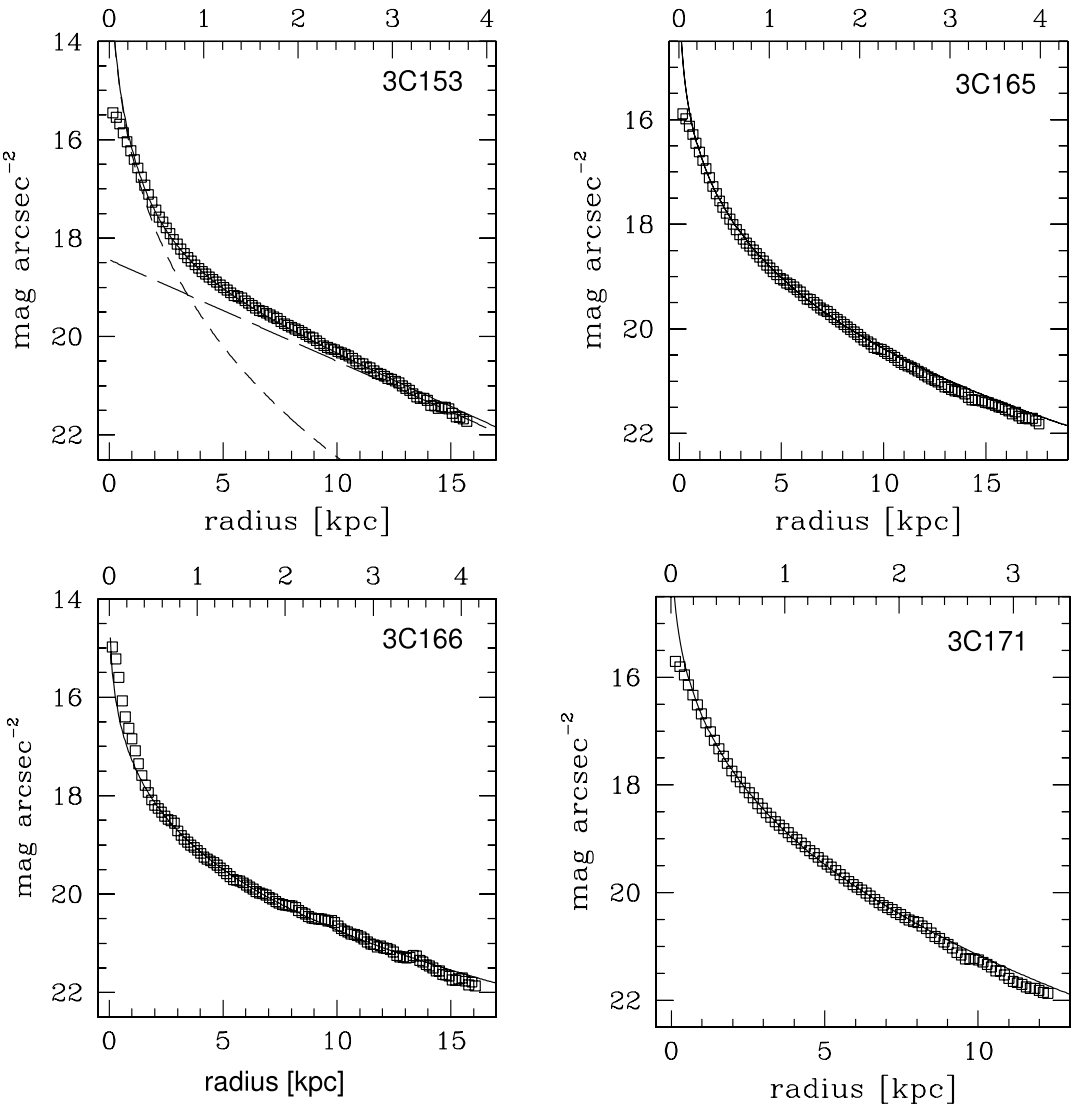

FIG. 1—*Continued*

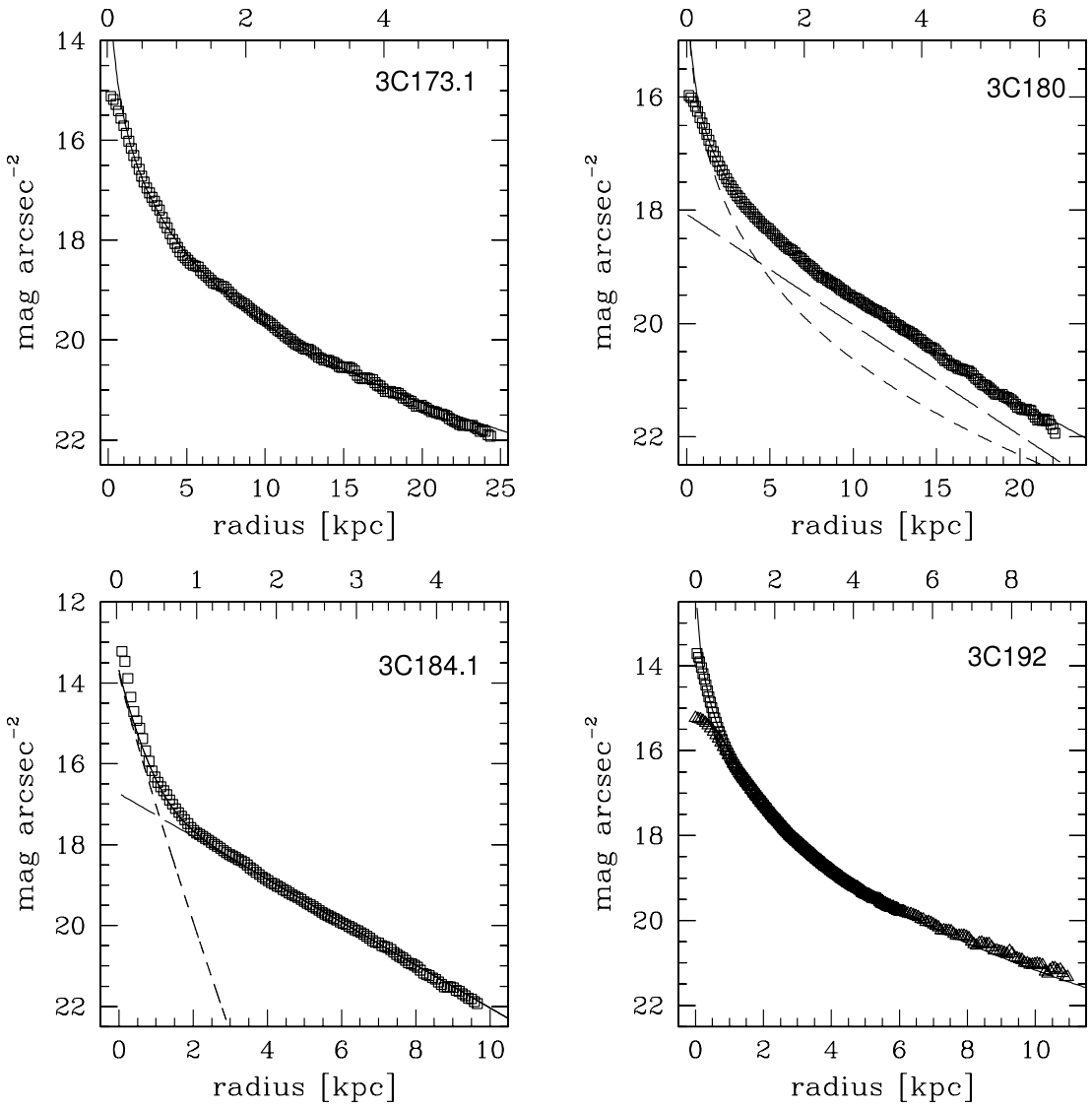

FIG. 1—*Continued*

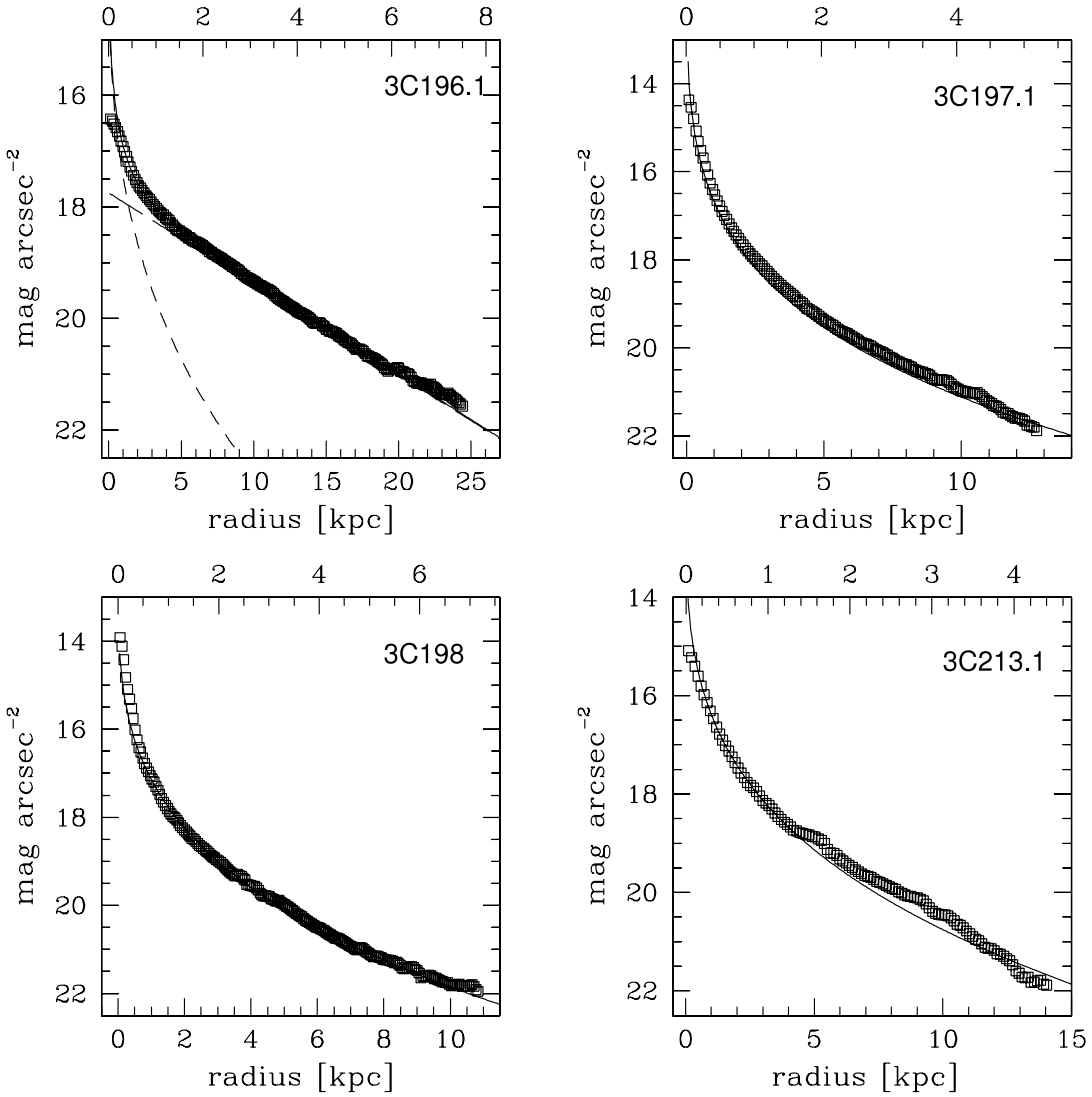

FIG. 1—*Continued*

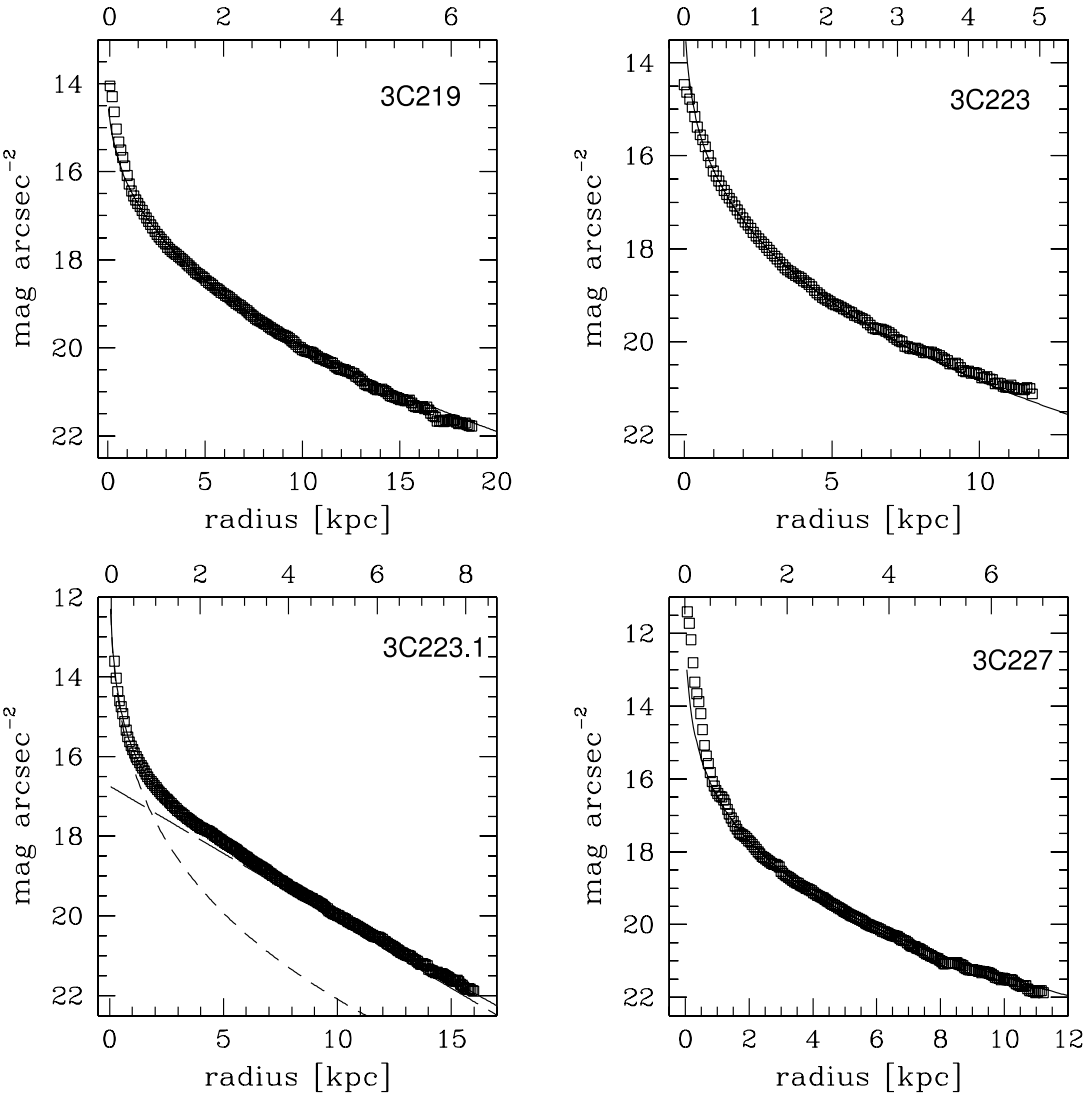

FIG. 1—*Continued*

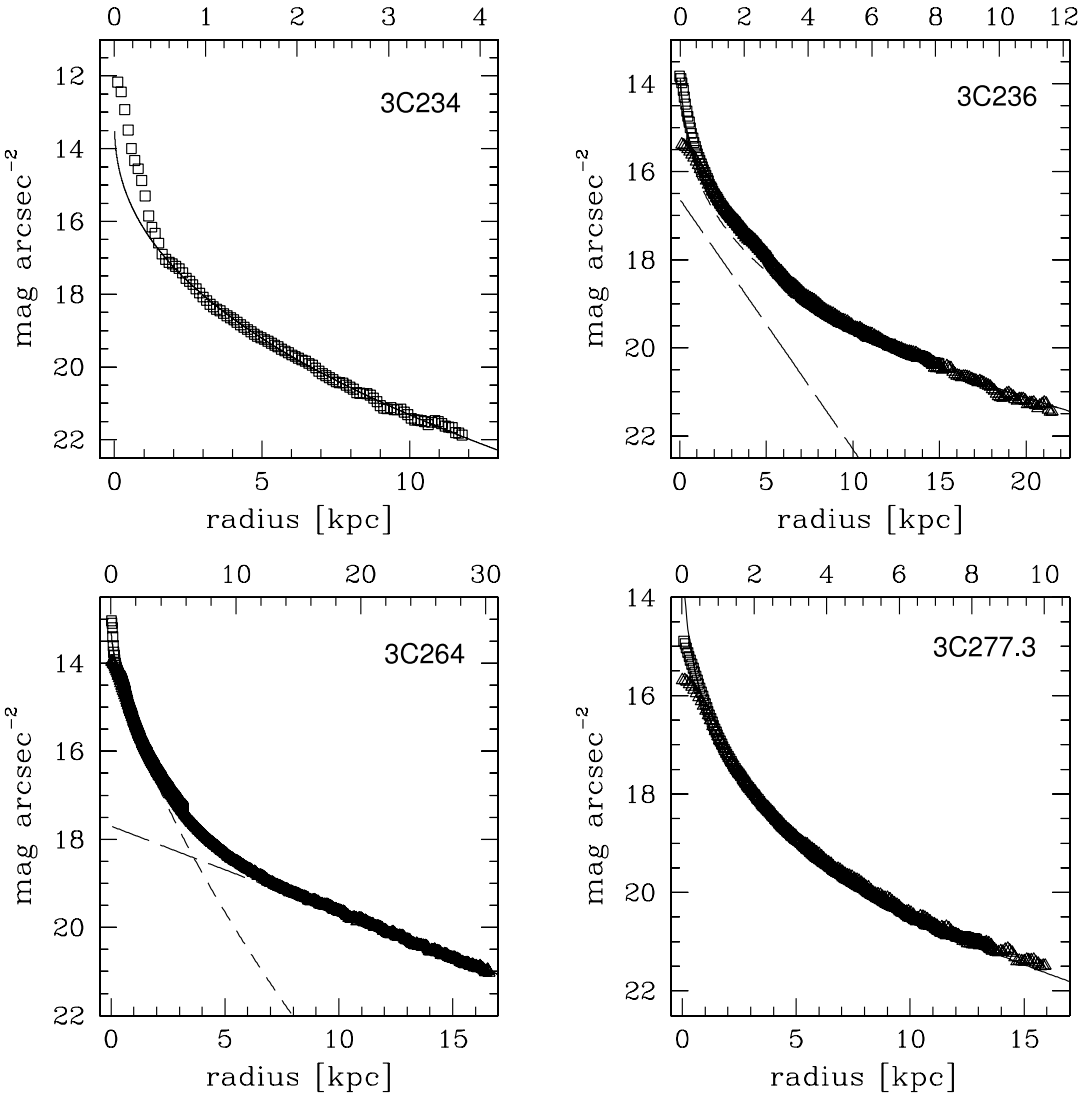

FIG. 1—*Continued*

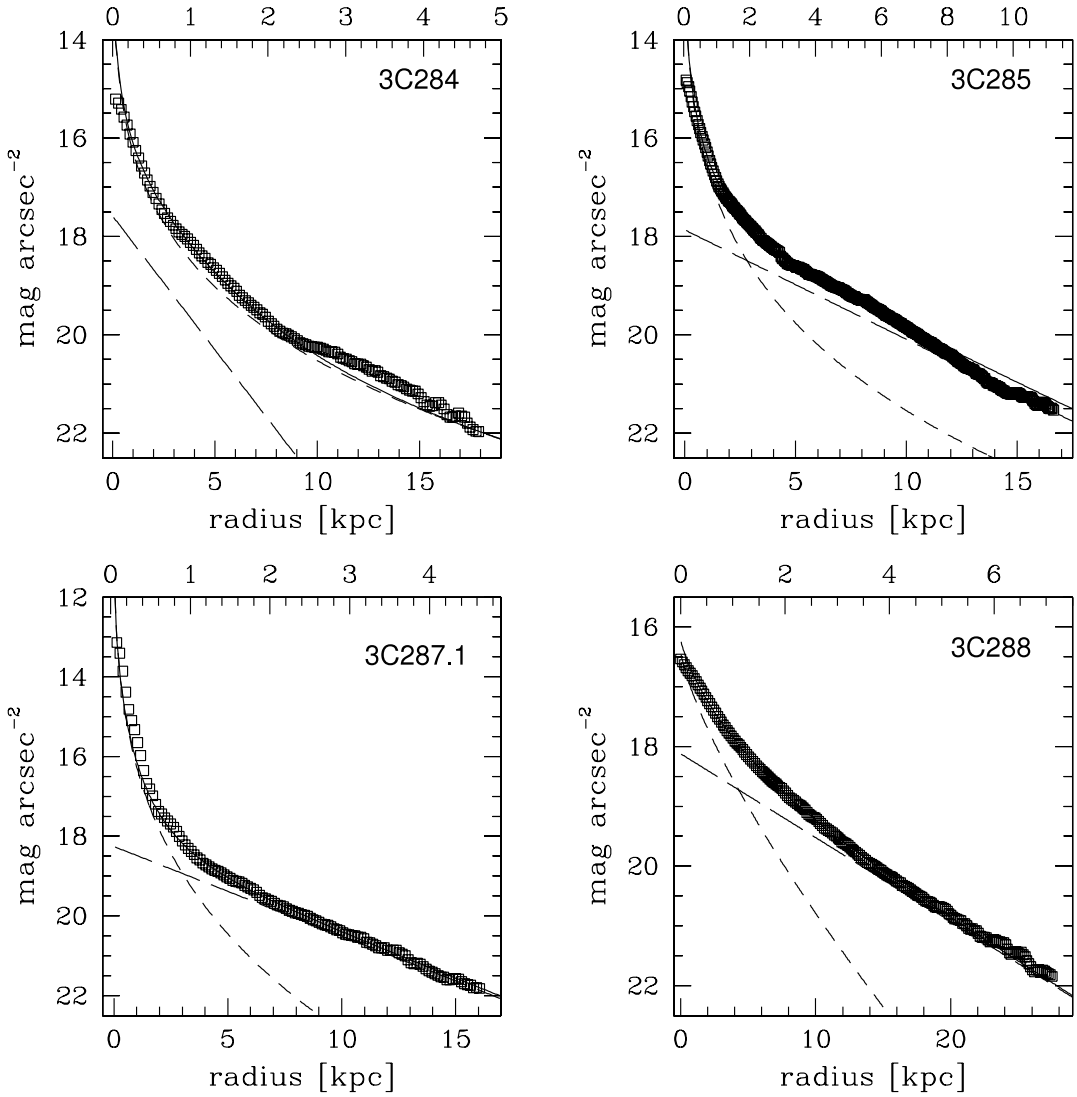

FIG. 1—*Continued*

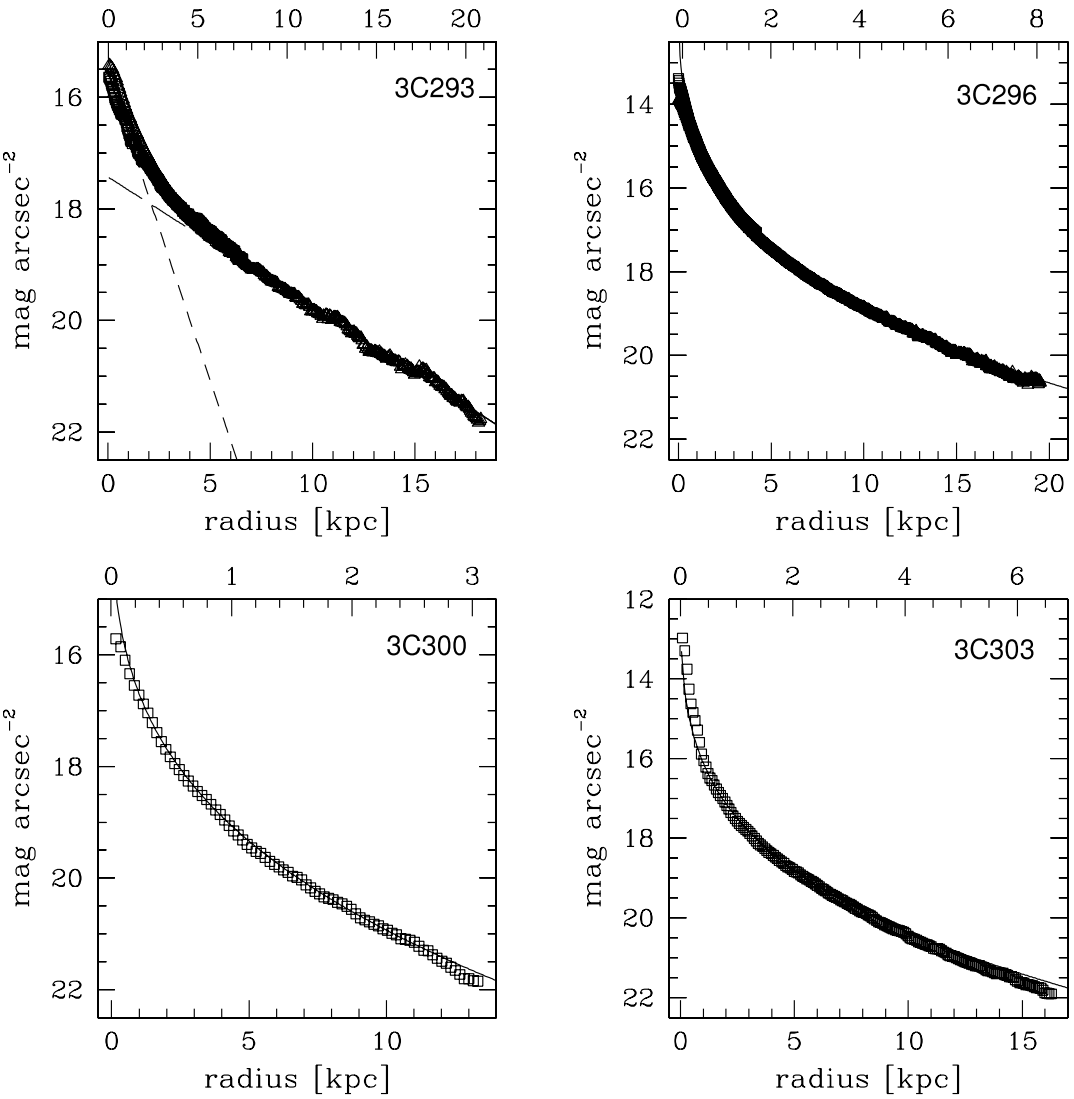

FIG. 1—*Continued*

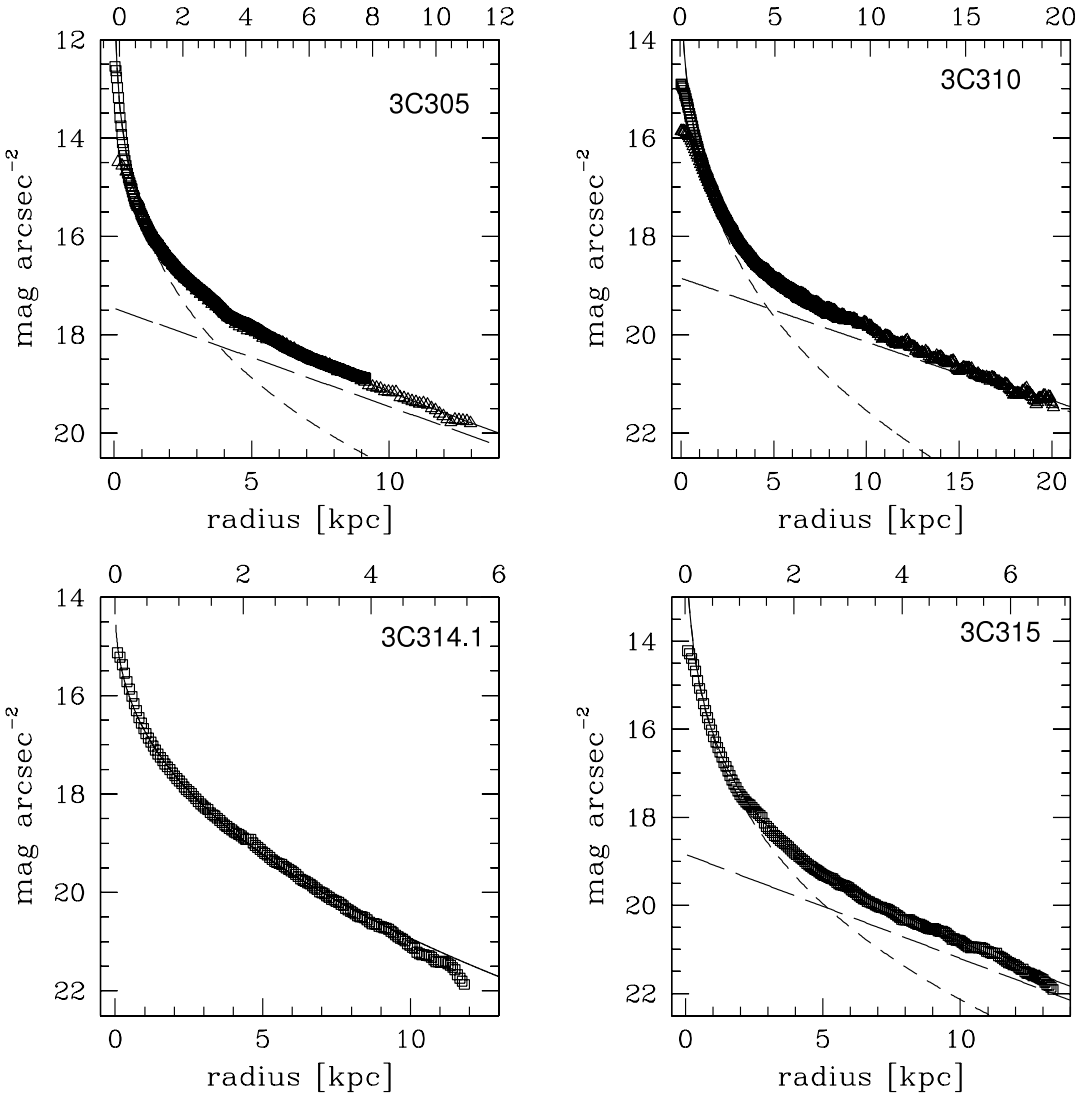

FIG. 1—*Continued*

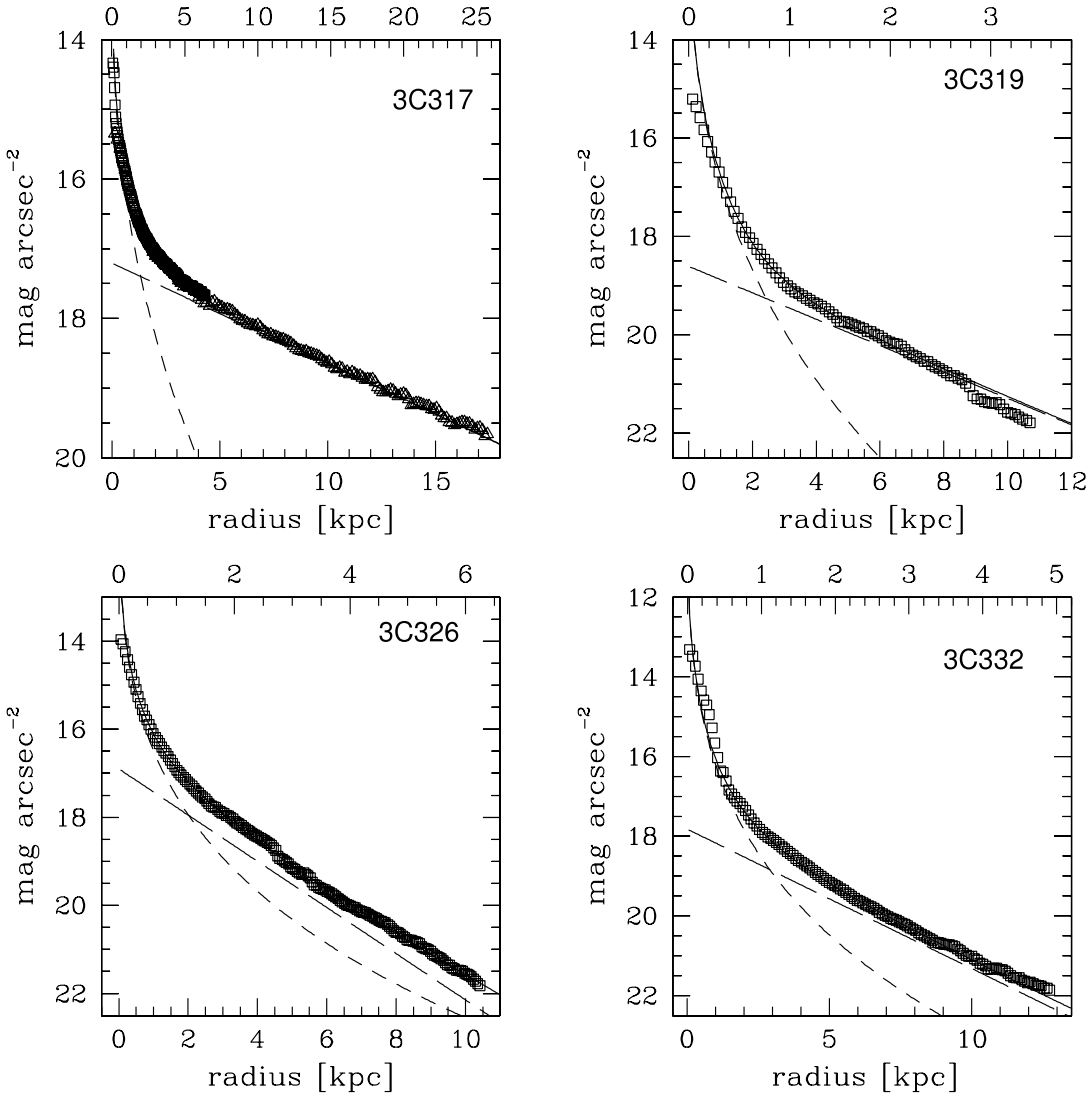

FIG. 1—*Continued*

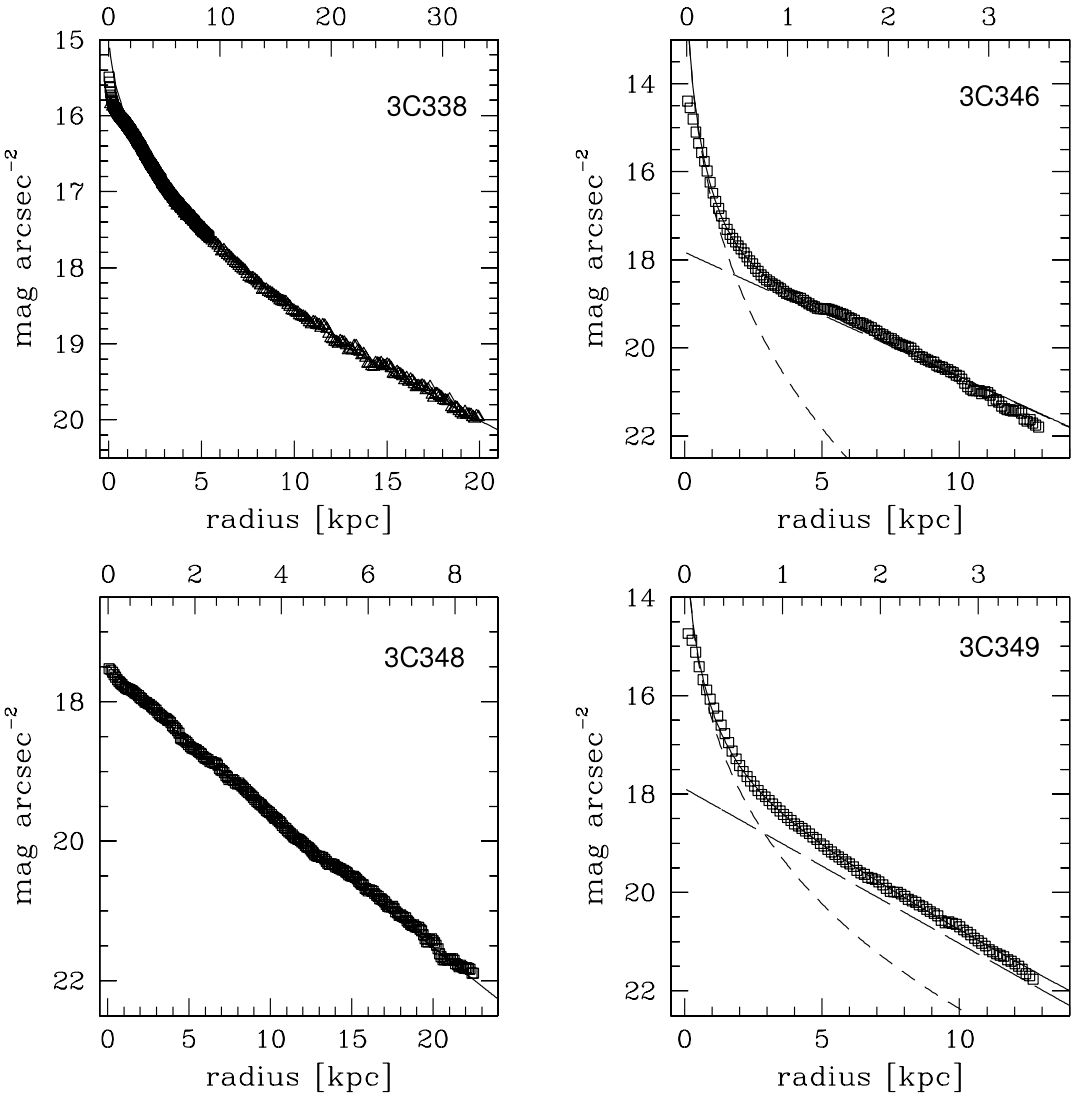

FIG. 1—*Continued*

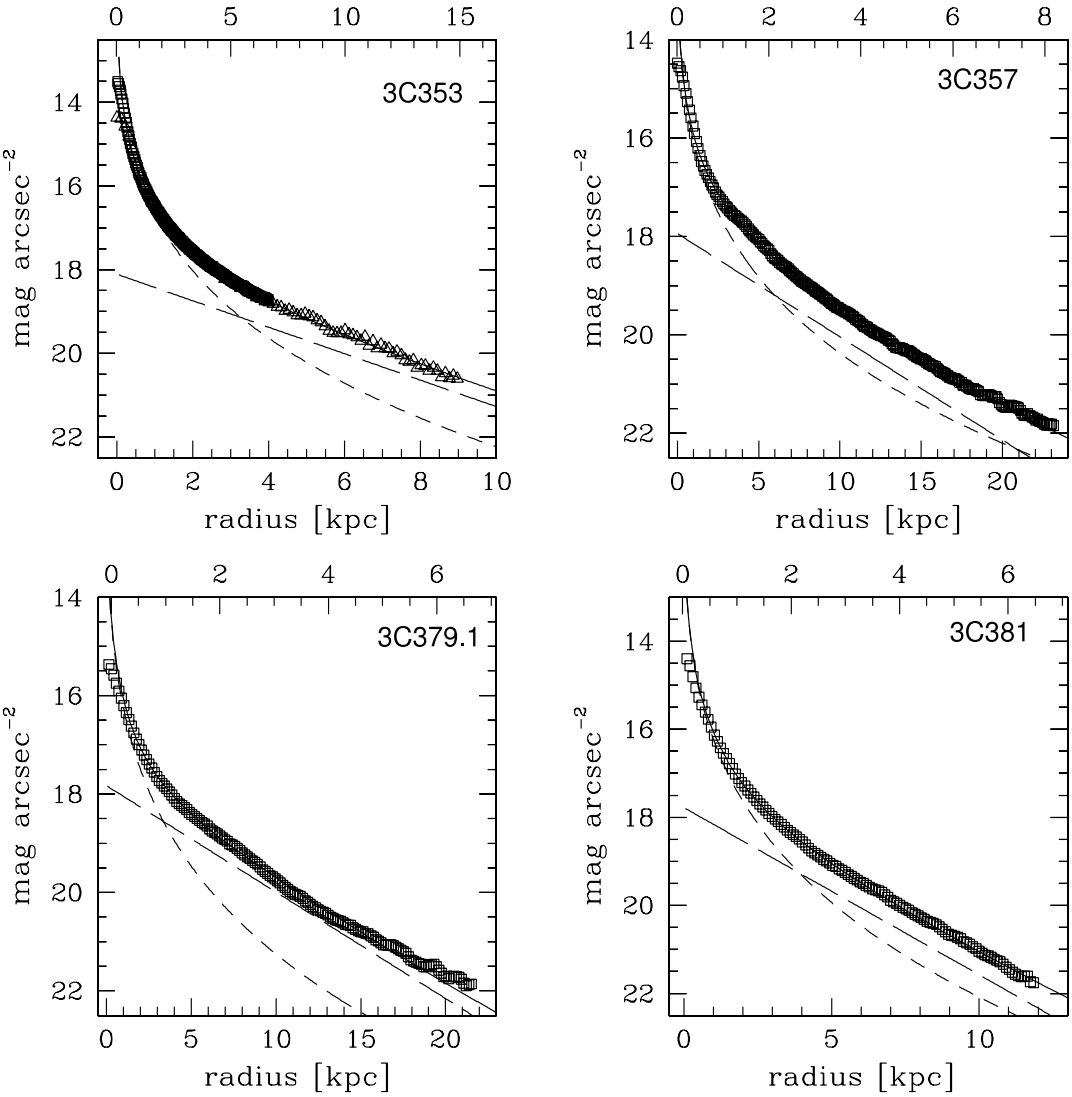

FIG. 1—*Continued*

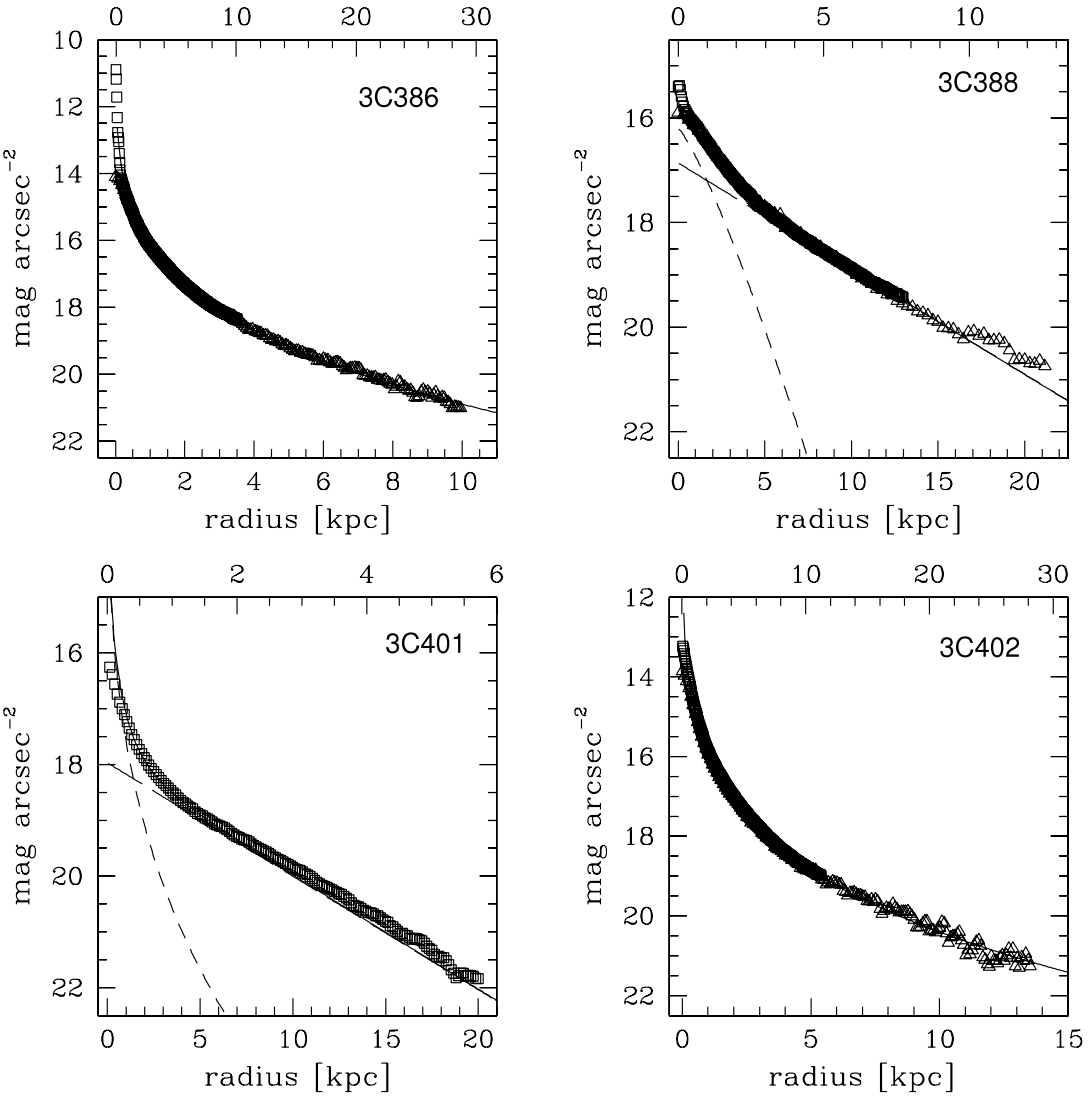

FIG. 1—*Continued*

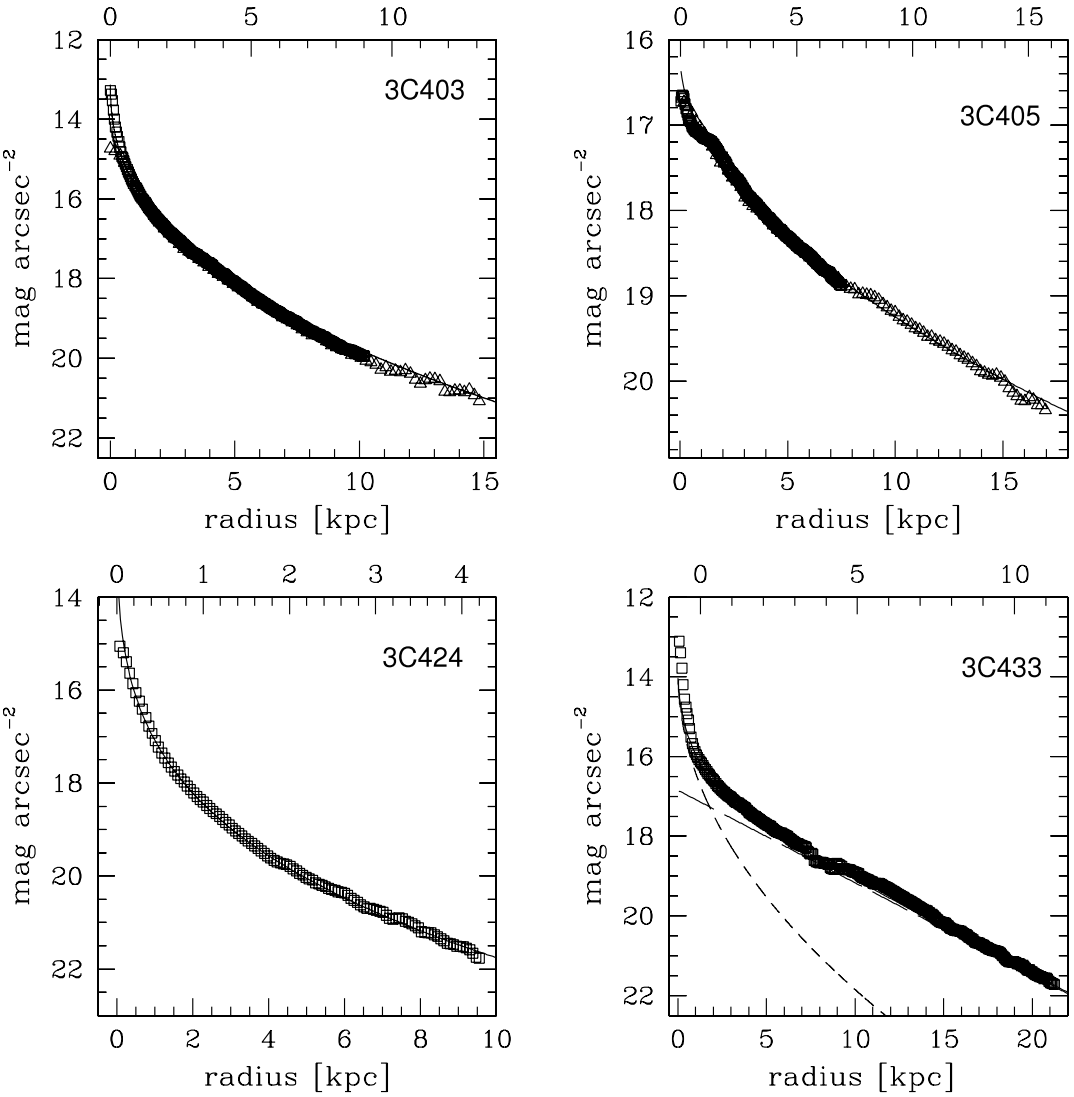

FIG. 1—*Continued*

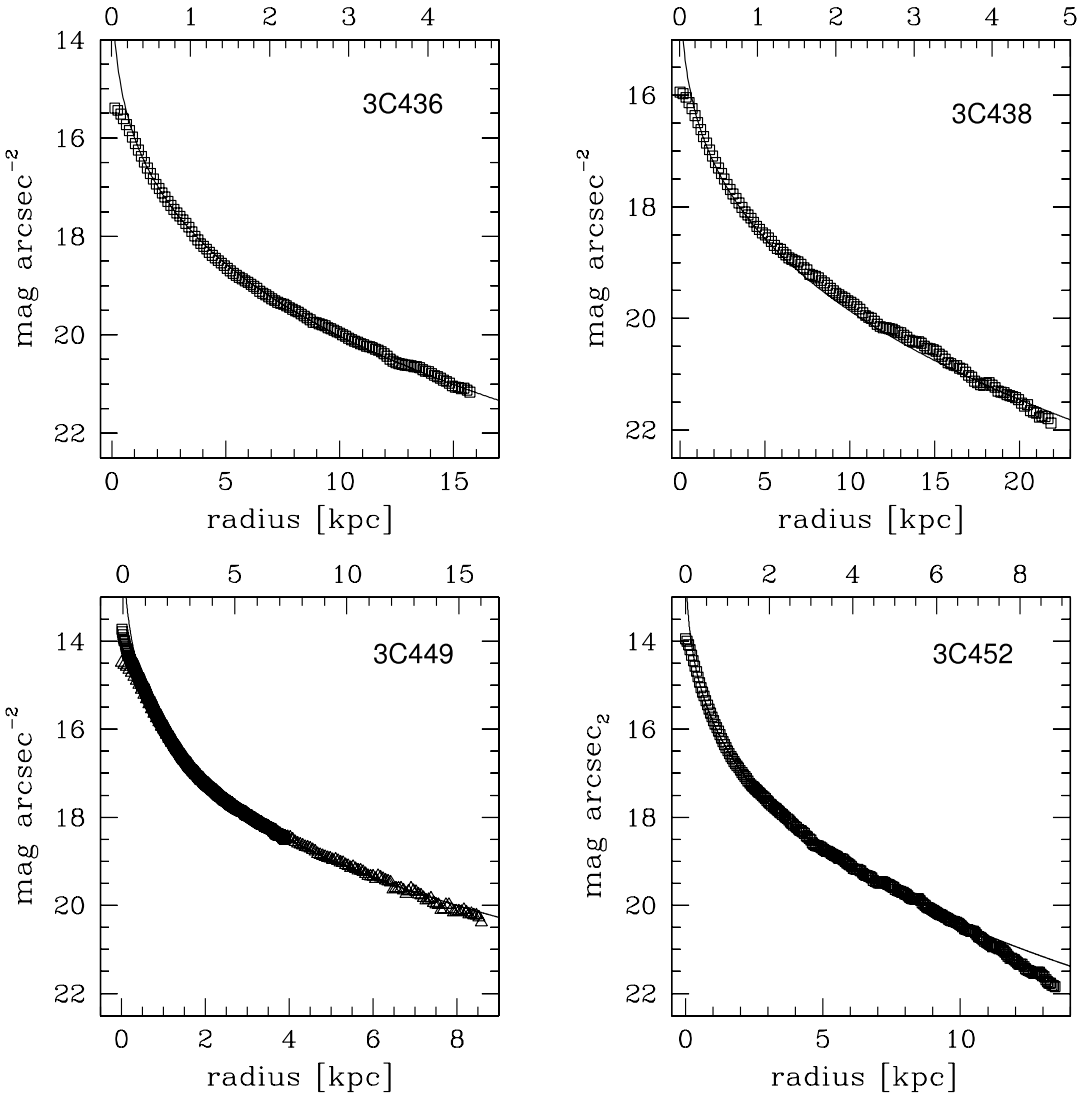

FIG. 1—*Continued*

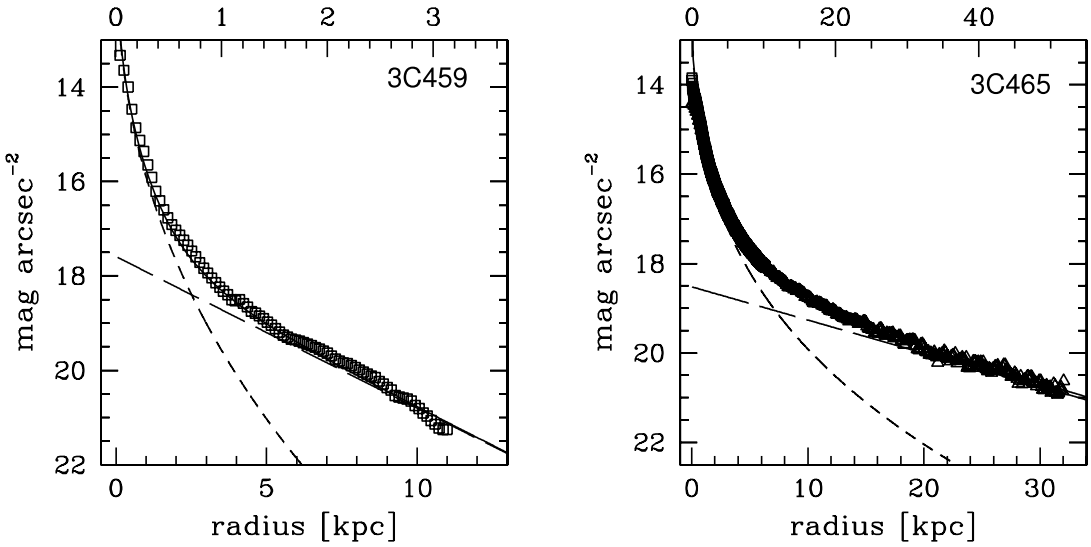

FIG. 1—*Continued*

for the exponential component. Here $\Gamma(2/\beta)$ is the Gamma function. Note that equation (2) assumes that the galaxy is face-on. Therefore, the intensities in equation (1) were corrected by inclination as in Kent (1985). Total apparent magnitudes were then converted into absolute magnitudes. Throughout this paper we assume a Hubble constant $H_0 = 71$ km s^{-1} Mpc^{-1} together with $\Omega_M = 0.27$ and $\Omega_\Lambda = 0.73$.

5. RESULTS AND DISCUSSION

Table 2 lists the photometric parameters obtained through the procedures described in the previous sections for all sample galaxies. Columns (1), (2), and (3) list the source name, ellipticity, and redshift, respectively. Ellipticity values correspond to the outermost isophotes and were taken from the tables generated by the `ellipse` routine. The bulge parameters μ_e, r_e, and n are listed in columns (4), (5), and (6), while columns (7) and (8) list disklike-component parameters μ_0 and r_0. The parameter μ_e was calculated using MH01 expression (6), given in § 4.1 of that paper. Finally, columns (9), (10), (11), and (12) list the bulge absolute magnitudes, disklike-component absolute magnitudes, total galaxy magnitudes, and bulge–to–disklike component ratio.

Forty-three out of 82 galaxies (52%) show a single Sérsic luminosity profile type. The remaining 39 galaxies (48%) have luminosity profiles that have to be fitted with a combination of a Sérsic profile plus an exponential profile. Among FR Is, 10 out of 22 galaxies (45%) show single luminosity profiles, while 12 (55%) show bulge+exponential type profiles. FR IIs show 33 out of 60 galaxies (55%) with single Sérsic luminosity profiles, and 27 galaxies (45%) with bulge+exponential type profiles. However, we also have four interesting cases: 3C 28, 3C 129.1, 3C 184.1, and 3C 388. These galaxies show $n > 0.75$. This is somewhat reminiscent of the so-called pseudobulges recently discovered in some spiral galaxies. Pseudobulges are formed through secular evolution of galaxies. In other words, the bulge is formed from disk evolution, allowing the direct formation of bulges from disks in isolated galaxies (Kormendy & Kennicutt 2004). Unfortunately, we do not have enough information, such as velocity dispersions, to confirm this possibility. 3C 348 is another interesting case since this galaxy has a single Sérsic profile with $n = 0.93$, which indicates it is a bulgeless galaxy. This result is unexpected since, as was pointed out in § 2, most of these galaxies are simply reported in the literature as ellipticals. However, it is not clear whether or not the exponential profile is the signature of a disk in all of them. To investigate whether these are real disks, we have plotted in Figures 2*a*–2*d* the distribution of ellipticity e for all galaxies of the sample. We differentiate between galaxies that show a single Sérsic luminosity profile and those that show bulge+exponential luminosity profiles, and also between galaxies classified as FR Is and FR IIs. Histograms are plotted in bins of $\Delta e = 0.05$. Galaxies that show a single luminosity profile (Fig. 2*d*) display a distribution in ellipticity that is rather similar to that displayed by a population of normal elliptical galaxies, which has been shown to peak at $e \sim 0.15$ (Sandage et al. 1970; Ryden 1992). For such a subsample we obtain an average ellipticity $e = 0.18 \pm 0.08$. The average ellipticity for galaxies that also show an exponential component in their luminosity profiles (Fig. 2*d*, *dashed line*) is instead $e = 0.24 \pm 0.10$. A Kolmogorov-Smirnov (K-S) test applied to these subsamples indicates that these two data sets do not have different ellipticity distributions. We also note that there are no differences between FR I (Fig. 2*b*) and FR II (Fig. 2*c*) ellipticity distributions. We obtain $e = 0.21 \pm 0.11$ and 0.20 ± 0.12 for FR I and FR II galaxies, respectively.

Figure 3*a* shows the total absolute magnitude distribution for all galaxies of the sample. Again, we have differentiated between FR I (Fig. 3*b*) and FR II sources (Fig. 3*c*), and also between galaxies with a single Sérsic luminosity profile (Fig. 3*d*). Total luminosity distributions for all the classes look similar. For the whole sample the luminosity peaks at $M_{\rm total} = -25.4 \pm 0.7$, while for the FR I and FR II subsamples separately the values are $M_{\rm total\ FR\ I} = -25.6 \pm 0.7$ and $M_{\rm total\ FR\ II} = -25.3 \pm 0.6$. The K-S test applied to FR I and FR II data sets indicates that the magnitude distributions are not statistically different.

We have performed a similar analysis for bulge and disklike-component photometric parameters for the whole sample as well as for the FR I and FR II subsamples. The average values for the photometric parameters together with their standard deviations are listed in Table 3. FR I and FR II bulges have similar properties in terms of their photometric parameters, $M_{\rm bulge}$, μ_e, and r_e. The concentration index average value is $\beta = 0.40 \pm 0.18$ for FR I galaxies, while for the FR II subsample it is $\beta = 0.33 \pm 0.08$. However, the K-S test indicates that the distributions of the concentration index for the FR Is and FR IIs are not statistically different.

FR I and FR II disklike components show some interesting differences. As reported in Table 3, the FR Is' scale length (r_0)

TABLE 2

F160W Photometric Properties of the NICMOS Snapshot Survey

Source (1)	Ellipticity (2)	z (3)	μ_e (4)	r_e (5)	β (6)	μ_0 (7)	r_0 (8)	$M_{\rm bulge}$ (9)	$M_{\rm disklike\ component}$ (10)	$M_{\rm total}$ (11)	b/e (12)
3C 17	0.25	0.21968	18.28	3.21	0.370	...	...	−24.88	...	−24.88	...
3C 20	0.05	0.17400	17.89	2.33	0.350	...	...	−24.43	...	−24.43	...
3C 28	0.18	0.19520	17.76	1.05	0.821	17.25	4.49	−22.49	−25.36	−25.43	0.07
3C 31	0.11	0.01670	18.09	5.22	0.272	...	...	−25.50	...	−25.50	...
3C 33.1	0.09	0.18090	18.65	3.08	0.443	...	...	−24.16	...	−24.16	...
3C 35	0.27	0.06700	18.77	5.89	0.371	...	...	−25.13	...	−25.13	...
3C 52	0.31	0.28540	19.06	8.34	0.240	...	...	−26.63	...	−26.63	...
3C 61.1	0.07	0.18400	19.52	2.86	0.282	...	...	−23.40	...	−23.40	...
3C 66.B	0.15	0.02150	19.31	9.16	0.248	19.94	20.69	−25.58	−25.32	−26.21	1.27
3C 75.N	0.03	0.02315	17.10	1.98	0.247	...	...	−24.41	...	−24.41	...
3C 76.1	0.15	0.03240	16.70	1.08	0.261	19.15	5.19	−23.45	−23.05	−24.02	1.46
3C 79	0.10	0.25595	18.38	4.27	0.348	...	...	−25.56	...	−25.56	...
3C 83.1	0.25	0.02550	18.93	12.01	0.214	...	...	−26.63	...	−26.63	...
3C 84	0.22	0.01756	18.73	6.52	0.356	18.22	8.12	−25.33	−25.11	−25.98	1.23
3C 88	0.35	0.03022	19.18	4.92	0.227	18.11	6.57	−24.42	−24.68	−25.31	0.79
3C 98	0.15	0.03000	18.31	3.12	0.248	...	...	−24.28	...	−24.28	...
3C 105	0.28	0.08900	17.16	1.19	0.315	17.55	2.20	−23.45	−23.12	−24.05	1.35
3C 111	0.25	0.04850	18.87	3.44	0.173	...	...	−24.16	...	−24.16	...
3C 123	0.12	0.21770	22.28	28.65	0.166	...	...	−26.04	...	−26.04	...
3C 129	0.13	0.02080	17.39	1.75	0.637	17.71	4.22	−23.33	−24.01	−24.47	0.54
3C 129.1	0.24	0.02220	17.32	1.76	0.900	17.76	5.97	−23.32	−24.78	−25.03	0.26
3C 132	0.18	0.21400	18.66	5.36	0.362	...	...	−25.60	...	−25.60	...
3C 133	0.06	0.27750	19.44	4.74	0.319	...	...	−24.82	...	−24.82	...
3C 135	0.19	0.12530	17.12	1.19	0.223	17.42	2.49	−23.78	−23.64	−24.47	1.14
3C 153	0.11	0.27700	16.79	1.28	0.259	18.44	5.27	−24.75	−24.81	−25.53	0.95
3C 165	0.18	0.29570	20.21	9.23	0.241	...	...	−25.72	...	−25.72	...
3C 166	0.07	0.24500	21.49	14.18	0.225	...	...	−25.24	...	−25.24	...
3C 171	0.08	0.23840	19.11	4.21	0.305	...	...	−24.78	...	−24.78	...
3C 173.1	0.23	0.29210	19.46	9.01	0.162	...	...	−26.62	...	−26.62	...
3C 180	0.43	0.22000	20.00	7.44	0.242	18.07	5.56	−25.21	−25.09	−25.91	1.11
3C 184.1	0.27	0.11820	15.79	0.59	0.904	16.74	2.05	−22.87	−23.88	−24.24	0.39
3C 192	0.03	0.05980	17.84	2.61	0.253	...	...	−24.39	...	−24.39	...
3C 196.1	0.29	0.19800	19.03	2.41	0.337	17.75	6.65	−23.47	−25.72	−25.85	0.13
3C 197.1	0.08	0.13010	19.42	4.73	0.227	...	...	−24.51	...	−24.51	...
3C 198	0.15	0.08150	19.31	3.50	0.292	...	...	−23.61	...	−23.61	...
3C 213.1	0.39	0.19400	18.95	4.59	0.281	...	...	−25.01	...	−25.01	...
3C 219	0.23	0.17440	18.92	6.27	0.399	...	...	−25.48	...	−25.48	...
3C 223	0.18	0.13680	18.71	4.06	0.286	...	...	−24.76	...	−24.76	...
3C 223.1	0.45	0.10700	16.99	1.50	0.261	16.74	3.21	−24.25	−24.78	−25.30	0.61
3C 227	0.17	0.08610	18.47	2.93	0.235	...	...	−24.21	...	−24.21	...
3C 234	0.07	0.18500	17.88	2.78	0.433	...	...	−24.76	...	−24.76	...
3C 236	0.34	0.10050	19.57	10.06	0.291	16.62	1.91	−25.72	−23.75	−25.89	6.15
3C 264	0.05	0.02172	16.13	1.52	0.671	17.70	5.48	−24.37	−24.70	−25.30	0.74
3C 277.3	0.05	0.08570	19.11	5.54	0.255	...	...	−24.93	...	−24.93	...
3C 284	0.03	0.23900	19.44	6.13	0.213	17.59	2.00	−25.48	−23.42	−25.63	6.69
3C 285	0.42	0.07940	18.63	3.00	0.239	17.87	4.89	−24.08	−24.49	−25.05	0.69
3C 287.1	0.12	0.21590	16.24	1.00	0.268	18.26	4.83	−24.55	−24.58	−25.32	0.97
3C 288	0.03	0.24600	18.94	4.79	0.749	18.12	7.73	−24.81	−25.83	−26.19	0.39
3C 293	0.55	0.04503	17.44	1.63	0.968	17.43	4.65	−23.09	−24.66	−24.89	0.23
3C 296	0.21	0.02370	17.97	6.60	0.277	...	...	−26.17	...	−26.17	...
3C 300	0.29	0.27000	19.31	4.92	0.299	...	...	−24.92	...	−24.92	...
3C 303	0.10	0.14100	18.93	5.30	0.259	...	...	−25.19	...	−25.19	...
3C 305	0.35	0.04164	17.39	2.58	0.224	17.46	5.44	−24.88	−24.97	−25.67	0.92
3C 310	0.15	0.05350	18.09	2.56	0.285	18.85	8.40	−24.06	−24.55	−25.09	0.63
3C 314.1	0.41	0.11970	18.99	4.44	0.408	...	...	−24.43	...	−24.43	...
3C 315	0.35	0.10830	16.83	1.39	0.252	18.84	4.59	−24.28	−23.47	−24.70	2.11
3C 317	0.30	0.03446	17.83	1.63	0.434	17.24	7.63	−23.06	−25.89	−25.97	0.07
3C 319	0.24	0.19200	16.40	0.78	0.353	18.61	4.05	−23.59	−23.74	−24.42	0.87
3C 326	0.39	0.08900	17.13	1.38	0.269	16.90	2.07	−23.86	−23.62	−24.50	1.25
3C 332	0.05	0.15150	15.94	0.88	0.254	17.82	3.10	−24.35	−23.82	−24.87	1.63
3C 338	0.28	0.03035	19.03	12.86	0.474	...	...	−26.29	...	−26.29	...
3C 346	0.30	0.16100	14.90	0.46	0.270	17.83	3.82	−23.98	−24.29	−24.90	0.76
3C 348	0.22	0.15400	19.58	9.25	0.925	...	...	−25.16	...	−25.16	...
3C 349	0.48	0.20500	17.27	1.48	0.249	17.89	3.45	−24.20	−24.02	−24.87	1.18

TABLE 2—*Continued*

Source (1)	Ellipticity (2)	z (3)	μ_e (4)	r_e (5)	β (6)	μ_0 (7)	r_0 (8)	$M_{\rm bulge}$ (9)	$M_{\rm disklike\ component}$ (10)	$M_{\rm total}$ (11)	b/e (12)
3C 353	0.03	0.03043	17.86	1.85	0.251	18.11	3.43	−23.53	−23.24	−24.15	1.31
3C 357	0.32	0.16700	18.94	5.29	0.238	17.94	5.17	−25.34	−24.87	−25.88	1.54
3C 379.1	0.11	0.25600	18.14	2.77	0.225	17.83	5.02	−25.06	−25.22	−25.89	0.87
3C 381	0.17	0.16050	17.10	1.56	0.264	17.78	2.86	−24.43	−23.71	−24.88	1.95
3C 386	0.12	0.01700	18.32	3.38	0.226	...	...	−24.38	...	−24.38	...
3C 388	0.13	0.09100	17.64	2.21	1.227	16.86	5.37	−23.62	−25.71	−25.86	0.14
3C 401	0.18	0.20104	17.89	1.17	0.310	17.97	5.34	−22.95	−24.89	−25.06	0.17
3C 402	0.21	0.02390	18.85	5.00	0.190	...	...	−24.76	...	−24.76	...
3C 403	0.26	0.05900	18.01	4.72	0.405	...	...	−25.32	...	−25.32	...
3C 405	0.25	0.05608	20.01	14.85	0.525	...	...	−25.67	...	−25.67	...
3C 424	0.03	0.12699	19.38	3.67	0.254	...	...	−23.91	...	−23.91	...
3C 433	0.43	0.10160	17.90	2.51	0.494	16.85	4.68	−24.08	−25.44	−25.71	0.29
3C 436	0.18	0.21450	19.12	6.61	0.255	...	...	−25.75	...	−25.75	...
3C 438	0.10	0.29000	19.86	9.96	0.298	...	...	−26.06	...	−26.06	...
3C 449	0.48	0.01710	19.01	5.08	0.164	...	...	−24.75	...	−24.75	...
3C 452	0.24	0.08110	18.15	3.83	0.276	...	...	−25.00	...	−25.00	...
3C 459	0.15	0.21990	15.45	0.81	0.430	17.59	3.38	−24.63	−24.48	−25.31	1.14
3C 465	0.20	0.03030	17.67	3.92	0.311	18.52	14.59	−25.25	−25.98	−26.43	0.51

NOTES.—Col. (1): 3CR number. Col. (2): Ellipticity. Col. (3): Redshift. Col. (4): Effective surface magnitude. Col. (5): Effective radius. Col. (6): Concentration index. Col. (7): Central surface magnitude. Col. (8): Scale length. Col. (9): Bulge absolute magnitude. Col. (10): Disklike-component absolute magnitude. Col. (11): Total absolute magnitude. Col. (12): Bulge/disklike component ratio.

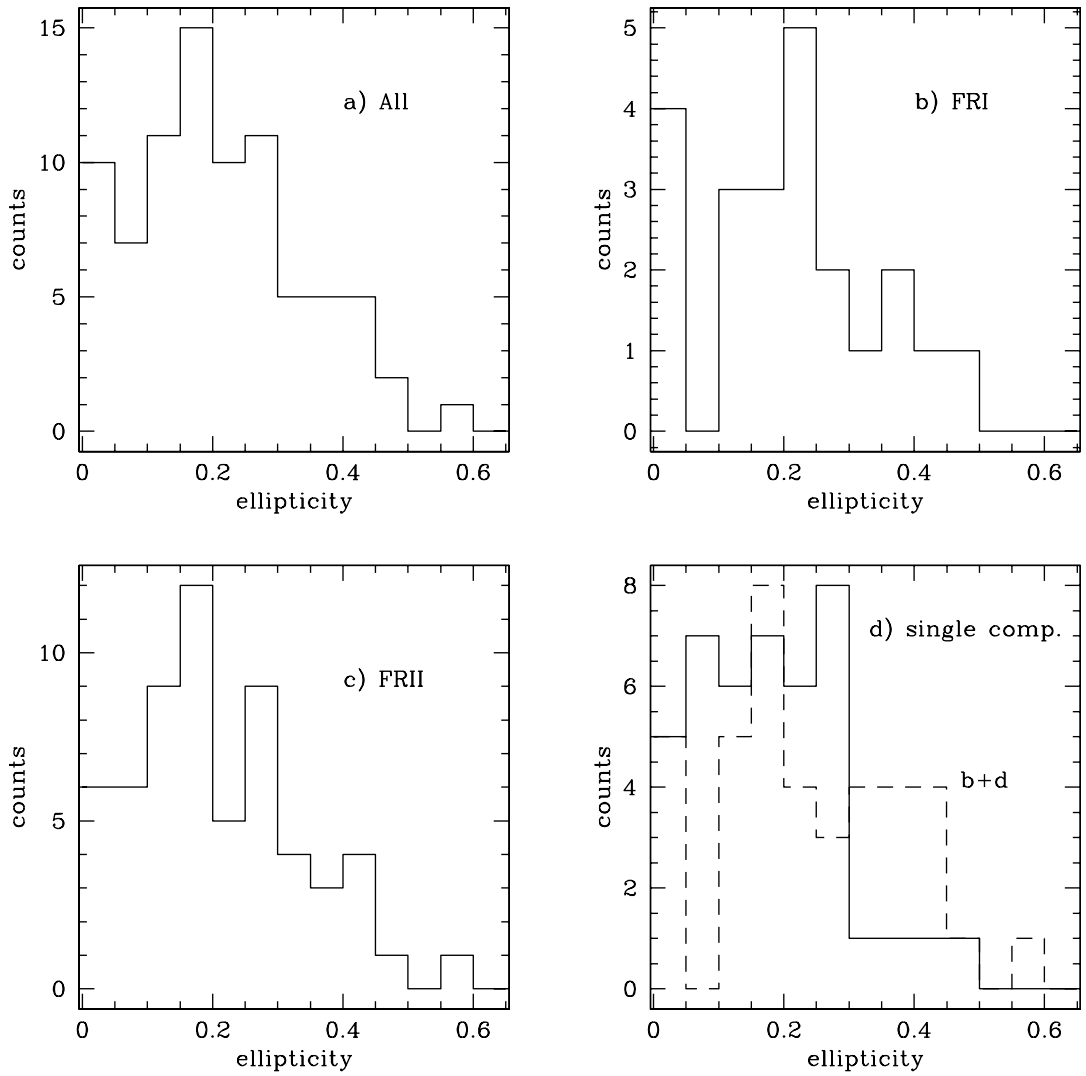

FIG. 2.—Ellipticity distributions for (*a*) whole sample, (*b*) FR I galaxies, (*c*) FR II galaxies, and (*d*) galaxies with a single Sérsic luminosity profile (*solid histogram*) and bulge+disklike component luminosity profile galaxies (*dashed histogram*).

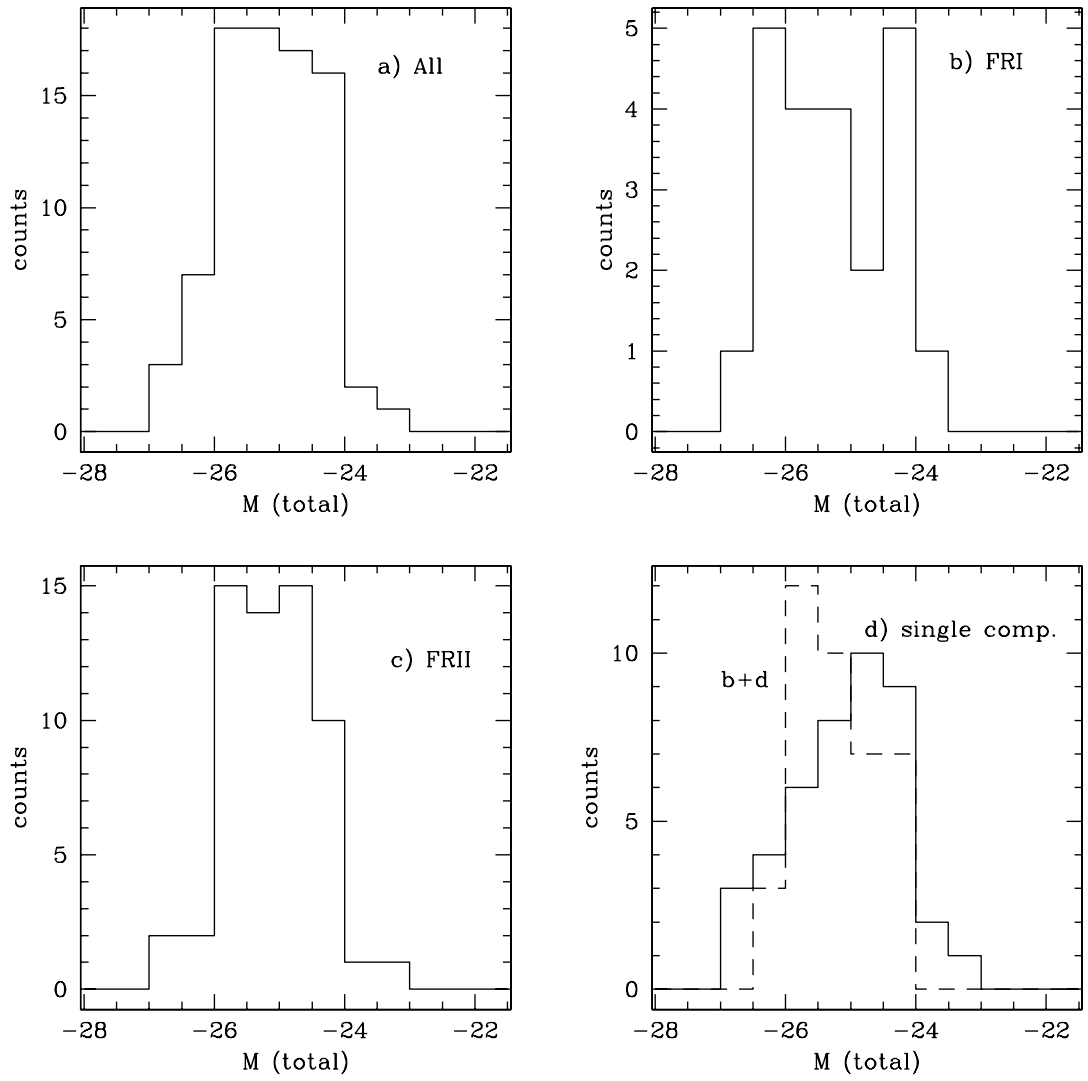

FIG. 3.—Total luminosity distributions for (*a*) whole sample, (*b*) FR I galaxies, (*c*) FR II galaxies, and (*d*) galaxies with a single Sérsic luminosity profile (*solid histogram*) and bulge+disklike component luminosity profile galaxies (*dashed histogram*).

is on average a factor of 2 larger than that of FR IIs, although the spread in r_0 is large; thus they are consistent within 1 σ. Similarly, the central surface magnitude (μ_0) is 0.6 mag dimmer in FR I galaxies, but again consistent with that of FR IIs within 1 σ. Interestingly, the K-S tests applied to these data indicate that the μ_0 and r_0 distributions are statistically different at 98% and 99.9% confidence levels for FR I and FR II galaxies, respectively. We also find that the mean total disklike component magnitudes are $M_{\text{disklike component FR I}} = -25.1 \pm 0.6$ and $M_{\text{disklike component FR II}} = -24.6 \pm 0.6$. However, in this case the K-S test does not indicate that the distributions are statistically different.

Finally, the bulge–to–disklike component luminosity ratio is $b/e = 0.8 \pm 0.4$ for FR Is while it is $b/e = 1.3 \pm 0.8$ for FR IIs. The K-S test does not indicate that these data sets are statistically different.

5.1. *Correlation of Structural Parameters*

The study of correlations between photometric parameters is a good tool for understanding the structure of galaxies and

TABLE 3
AVERAGE PARAMETERS FOR FR I AND FR II GALAXIES

Galaxies (1)	M_{total} (2)	M_{bulge} (3)	$M_{\text{disklike component}}$ (4)	μ_e (mag arcsec^{-2}) (5)	r_e (kpc) (6)	β (7)	μ_0 (mag arcsec^{-2}) (8)	r_0 (kpc) (9)	b/e (10)
All	-25.4 ± 0.7	-25.0 ± 0.9	-24.8 ± 0.6	17.6 ± 1.1	4.6 ± 2.7	0.35 ± 0.18	17.6 ± 0.7	5.3 ± 2.8	1.1 ± 1.0
FR I.....	-25.6 ± 0.7	-25.1 ± 0.9	-25.1 ± 0.6	17.7 ± 0.8	4.7 ± 2.6	0.40 ± 0.18	18.1 ± 0.7	8.2 ± 2.7	0.8 ± 0.4
FR II.....	-25.3 ± 0.6	-25.0 ± 0.7	-24.6 ± 0.6	17.5 ± 1.0	4.6 ± 2.6	0.33 ± 0.08	17.5 ± 0.4	4.0 ± 1.3	1.3 ± 0.8

NOTES.—Col. (1): Subsample galaxies. Col. (2): Total absolute magnitude. Col. (3): Bulge total magnitude. Col. (4): Disklike-component total magnitude. Col. (5): Bulge effective magnitude. Col. (6): Bulge effective radius. Col. (7): Concentration index. Col. (8): Disklike-component central surface magnitude. Col. (9): Disklike-component scale length. Col. (10): Bulge–to–disklike component ratio.

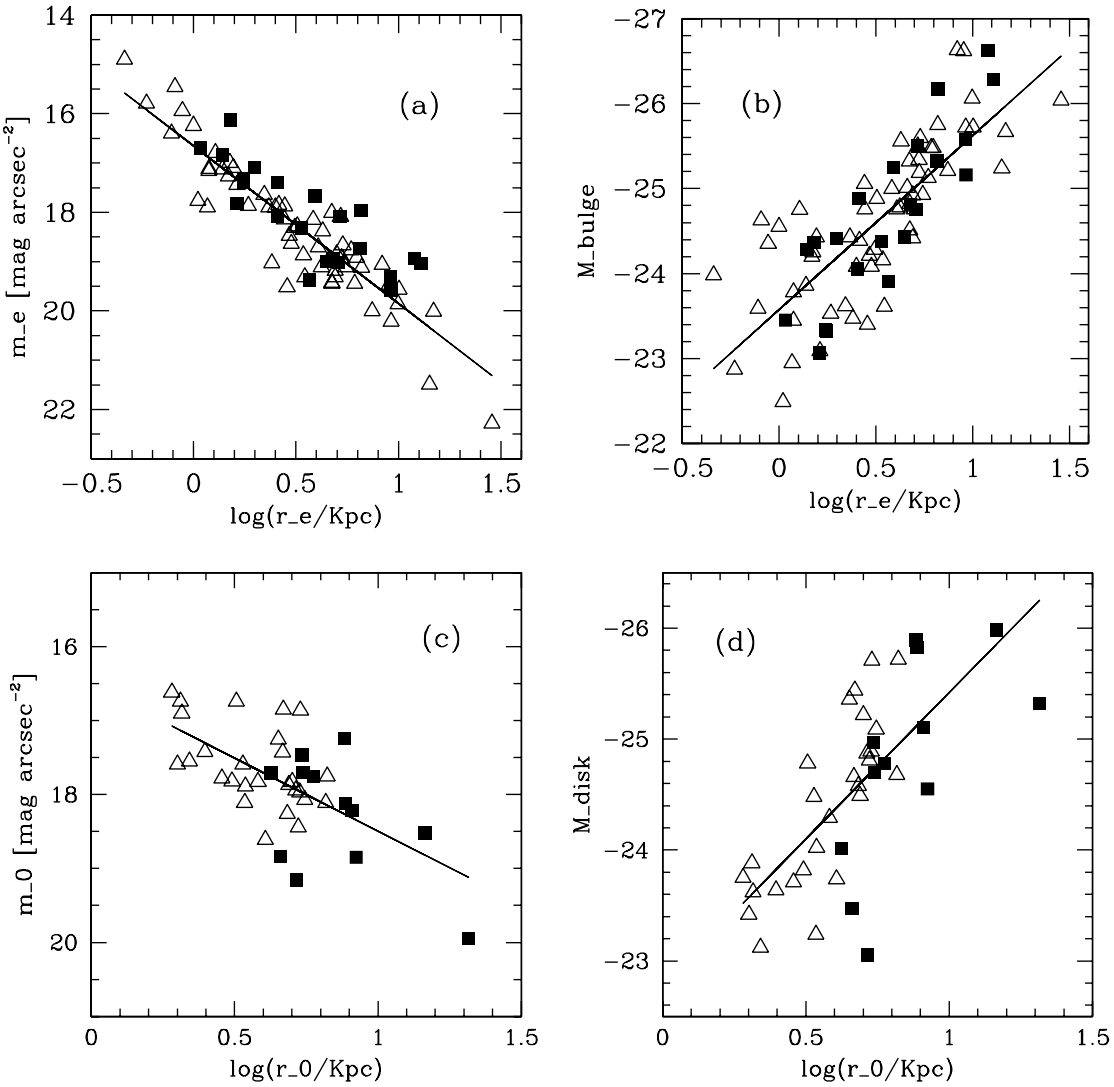

FIG. 4.— Photometric correlations. (*a*) Effective magnitude vs. log of the effective radius. (*b*) Bulge luminosity vs. log of the effective radius. (*c*) Central surface magnitude vs. log of the scale length. (*d*) Disklike-component total luminosity vs. log of the scale length. Squares represent FR I galaxies while triangles represent FR II galaxies. Lines show the result of the linear regression.

their evolution. Many scaling relations for galaxies have been discovered this way, such as the fundamental plane (Djorgovski & Davis 1987, Dressler et al. 1987) for elliptical galaxies and the Tully-Fisher (1977) relation for spirals.

The correlations between structural parameters for both bulges and disklike components obtained for our sample are plotted in Figure 4. Open triangles represent FR IIs while filled squares represent FR Is. Figures 4*a* and 4*b* show the effective surface magnitude (μ_e) and the bulge total absolute magnitude ($M_{\rm bulge}$) plotted against the logarithm of the effective radius (r_e) in kiloparsecs. From these plots we see a clear correlation between these parameters, in the sense that large bulges have lower effective surface magnitudes and higher total luminosities. The first correlation is the Kormendy relation (Kormendy 1977) for bulge galaxies. A linear regression applied to these data gives

$$\mu_e = 16.6(\pm 0.2) + 3.2(\pm 0.3)\log(r_e/\mathrm{kpc}),$$
$$M_{\rm bulge} = -23.6(\pm 0.3) - 2.0(\pm 0.4)\log(r_e/\mathrm{kpc}).$$

The slope for the μ_e versus r_e regression is quite similar to that obtained by Veilleux et al. (2006) for a sample of 33 luminous, late-stage galactic mergers and also to that obtained by Dunlop et al. (2003) for their subsample of radio-loud quasars. The μ_e versus r_e relationship for these types of galaxies shows a steeper slope than that found for normal ellipticals, $\sim$1.8 (Pahre 1999).

When this analysis is only applied to FR Is we obtain

$$\mu_e = 16.7(\pm 0.3) + 2.5(\pm 0.5)\log(r_e/\mathrm{kpc}),$$
$$M_{\rm bulge} = -23.2(\pm 0.3) - 2.6(\pm 0.5)\log(r_e/\mathrm{kpc}),$$

while for FR IIs we have

$$\mu_e = 16.7(\pm 0.2) + 3.4(\pm 0.4)\log(r_e/\mathrm{kpc}),$$
$$M_{\rm bulge} = -23.7(\pm 0.4) - 1.9(\pm 0.6)\log(r_e/\mathrm{kpc}).$$

These results indicate that FR Is and FR IIs have similar Kormendy and $M_{\rm bulge}$ versus log (r_e) relations, which is in agreement with the results of Dunlop et al. (2003). These authors find similar Kormendy relations for a sample of 13 radio-quiet quasars, 10 radio-loud quasars, and 10 radio galaxies.

We also investigate the correlations for disklike-component photometric parameters. The results are shown in Figures 4*c* and 4*d*.

TABLE 4
AVERAGE PARAMETERS FOR FR I, LEG, HEG, AND QSO GALAXIES

Galaxies (1)	M_{total} (2)	M_{bulge} (3)	$M_{disklike\ component}$ (4)	μ_e (mag arcsec^{-2}) (5)	r_e (kpc) (6)	β (7)	μ_0 (mag arcsec^{-2}) (8)	r_0 (kpc) (9)	b/e (10)
FR I.....	-25.6 ± 0.7	-25.1 ± 0.7	-25.1 ± 0.7	17.7 ± 0.9	4.7 ± 2.6	0.40 ± 0.16	18.1 ± 0.6	8.2 ± 3.1	0.8 ± 0.4
LEG.....	-25.5 ± 0.6	-25.2 ± 0.9	-24.7 ± 0.6	17.7 ± 1.4	5.8 ± 4.1	0.38 ± 0.10	17.5 ± 0.5	4.3 ± 1.1	1.2 ± 0.8
HEG.....	-25.2 ± 0.5	-24.9 ± 0.6	-24.5 ± 0.7	18.1 ± 0.8	4.2 ± 2.0	0.29 ± 0.10	17.5 ± 0.3	3.6 ± 1.1	1.6 ± 0.9
QSO.....	-25.0 ± 0.5	-24.7 ± 0.6	-24.8 ± 0.8	17.3 ± 0.7	3.1 ± 1.2	0.36 ± 0.11	17.5 ± 0.4	4.2 ± 1.8	0.8 ± 0.5

NOTES.—Col. (1): Subsample galaxies. Col. (2): Total absolute magnitude. Col. (3): Bulge total magnitude. Col. (4): Disklike-component total magnitude. Col. (5): Bulge effective magnitude. Col. (6): Bulge effective radius. Col. (7): Concentration index. Col. (8): Disklike-component central surface magnitude. Col. (9): Disklike-component scale length. Col. (10): Bulge–to–disklike component ratio.

Disklike-component parameters show the same trend as seen for bulge parameters. More explicitly, large disklike components have a lower central surface magnitude and have higher total luminosities. However, in this case the data show a larger dispersion than that observed for the bulges. Linear regression fits applied to these data yield the following results:

$$\mu_0 = 16.5(\pm 0.3) + 2.0(\pm 0.5) \log (r_0/\mathrm{kpc}),$$
$$M_{\mathrm{disklike\ component}} = -22.8(\pm 0.2) - 2.6(\pm 0.6) \log (r_0/\mathrm{kpc}).$$

Intriguingly, these results are similar to those obtained by MH01 for the disk components of a sample of 40 bright spiral galaxies. This result could give further support to the idea that exponential profiles in these galaxies are truly due to the presence of a disk. However, as pointed out by de Jong et al. (2004), this exponential distribution of light might not be in a disk configuration flattened by rotation, as disks of spiral galaxies are.

6. FR Is, LEGs, HEGs, AND QSOs

The FR I and FR II classification is only based on the radio morphology of the source. We thus chose another classification scheme, one that relies on the spectroscopic properties and is more likely to reflect the physical properties of the central AGN. In particular, we adopt the scheme defined by Jackson & Rawlings (1997). They classify high- and low-ionization narrow-lined galaxies (HEGs and LEGs) on the basis of the equivalent width (EW) of the [O III] λ5007 emission line and/or the [O II]/[O III] ratio. Galaxies with [O II]/[O III] > 1 and/or EW < 10 Å are defined as LEGs (low-excitation galaxies). Similarly, quasars (QSOs) are defined as those sources for which at least one broad line has been observed. We find in our sample 22 FR Is (corresponding to 27% of the sample), 22 LEGs (27%), 24 HEGs (29%), and 13 QSOs (16%). Only two FR II objects remain unclassified (3C 277.3 and 3C 346). As we pointed out in § 5, 55% of FR I galaxies show bulge+exponential type profiles, which is identical to the percentage obtained for LEGs. HEGs show less galaxies with bulge+exponential profiles (43%), while for QSOs only 31% of the galaxies have the exponential component. It is interesting to note that while FR IIs can be classified as HEGs, LEGs, or QSOs, most, if not all, FR I galaxies are weak-lined LEGs (Hine & Longair 1979; Laing 1994).

Summarizing, we divide our objects into the following spectral classification scheme: FR Is, LEGs, HEGs, and QSOs, and we investigate the statistical properties of the host galaxies under this classification. Table 4 lists the photometric parameters for each of these galaxy classes. All of them have bulges with similar average photometric properties, and even if FR Is have on average greater concentration indexes ($\beta = 0.40$ vs. $\beta \sim 0.34$), the Kolmogorov-Smirnov test applied to these data does not indicate that the β distribution for FR I bulges is statistically different from that for LEGs, HEGs, or QSOs.

Differences between these classes arise when we compare envelope photometric parameters. FR Is have on average larger disklike components ($r_0 = 8.2$ kpc) and dimmer central surface magnitude ($\mu_0 = 18.1$) than those of LEGs ($\mu_0 = 17.5$, $r_0 = 4.3$), HEGs ($\mu_0 = 17.5$, $r_0 = 3.6$), and QSOs ($\mu_0 = 17.5$, $r_0 = 4.2$). However, K-S tests applied to the μ_0 distributions differentiate FR Is only from HEGs and QSOs (99% confidence level), and not from LEGs. The same tests applied to the r_0 data of these classes reveal that FR Is have a different distribution when compared with those of LEGs, HEGs, and QSOs (99% confidence level). In other words, these results are similar to those obtained in the previous section. They suggest that from a photometric point of view, FR Is are slightly different from LEGs, and these differences become stronger when FR Is are compared to HEGs and QSOs. We also ran statistical tests comparing FR Is + LEGs to HEGs + QSOs. The results were similar to those just described, but with slightly less statistical significance (98% level). We find that FR Is + LEGs have on average $\mu_0 = 17.8 \pm 0.5$ mag arcsec^{-2}

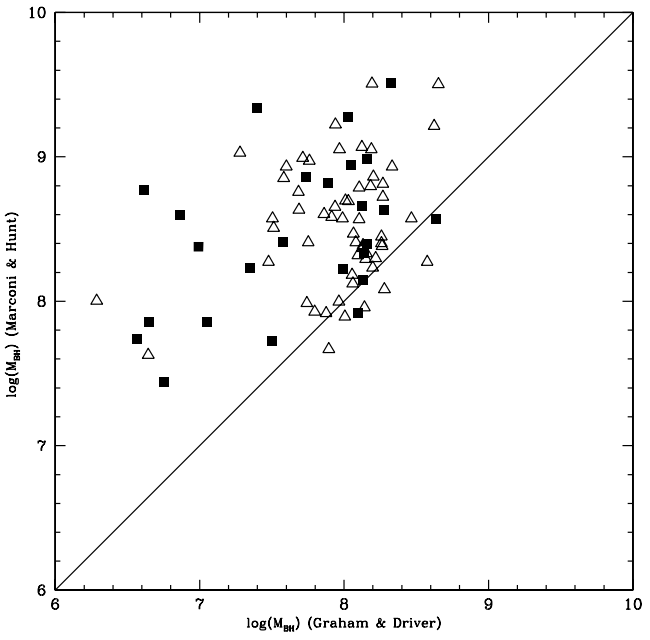

FIG. 5.—Black hole masses calculated for the sample galaxies. The x-axis shows the results obtained using the Graham & Driver (2007) relation while the y-axis shows masses obtained following the Marconi & Hunt (2003) relation. Squares and triangles represent FR I and FR II galaxies, respectively. The solid line indicates the $y = x$ function.

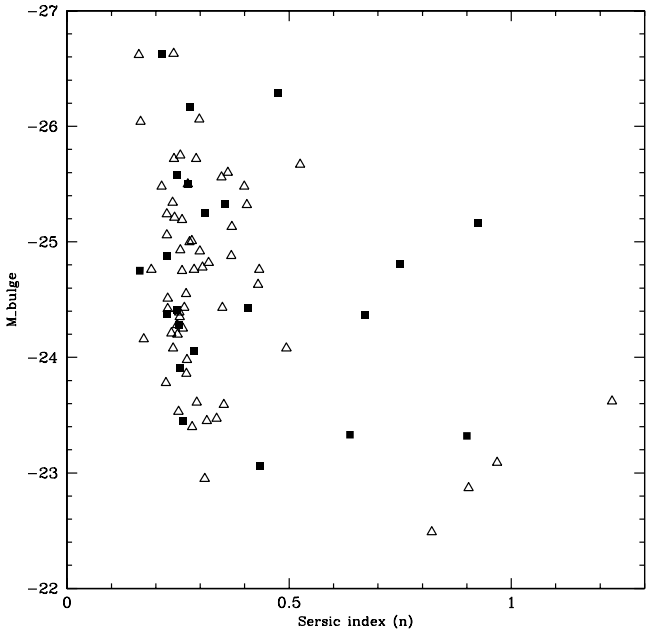

FIG. 6.—Total bulge luminosity vs. concentration index β. Squares and triangles represent FR I and FR II galaxies, respectively.

and $r_0 = 6.3 \pm 2.0$ kpc, while HEGs + QSOs have $\mu_0 = 17.5 \pm 0.4$ mag arcsec^{-2} and $r_0 = 3.9 \pm 1.2$ kpc.

7. BLACK HOLE MASS VERSUS BULGE NEAR-INFRARED LUMINOSITY AND SÉRSIC INDEX

Recent studies suggest that central super massive black holes (SMBHs) reside in all galaxies with a bulge, as a result of past quasar activity (Aller & Richstone 2002 and references therein). Moreover, SMBHs are claimed to be related to the host galaxy properties and therefore this implies that SMBHs and galaxy formation and evolution are closely correlated. Kormendy & Richstone (1995) showed that the mass of the SMBH is correlated (with considerable scatter) with both bulge luminosity and bulge mass. This result was later confirmed and strengthened by Magorrian et al. (1998) for a sample of nearby galaxies with kinematic data.

On the other hand, it has also been shown that $M_{\rm SMBH}$ correlates with the Sérsic index n (Graham et al. 2003 and references therein). These authors claim that the scatter of the $M_{\rm SMBH}$-n relation is equivalent to the $M_{\rm SMBH}$-σ relation (Ferrarese & Merrit 2000; Tremaine et al. 2002), and it has the additional advantage of requiring only galaxy images rather than spectra.

The superb quality of the *HST* NICMOS images, together with ground-based information for nearby objects, allows us to determine $L_{\rm bulge}$ and n with high accuracy. Therefore we can estimate the black hole mass for each galaxy of the sample using both relations, and check whether the results are consistent. First of all we use the following relation with $L_{\rm bulge}$, as taken from Marconi & Hunt (2003):

$$\log(M_{\rm SMBH}) = 8.04 + 1.25\left[\log(L_{H\,\rm bulge}) - 10.8\right],$$

where $M_{\rm SMBH}$ is the mass of the black hole and $L_{H\,\rm bulge}$ is the total bulge luminosity in the H band in solar units.

Second, we use the Graham & Driver (2007) relation:

$$\log(M_{\rm SMBH}) = 2.68\log(1/3\beta) + 7.82,$$

where β is the inverse of the Sérsic index as expressed in equation (1). We estimate the mass of the central black hole $M_{\rm SMBH}$ using the values of $M_{\rm bulge}$ and β as listed in Table 2, and the results are reported in Figure 5. In the figure, the triangles and squares represent FR I and FR II populations, respectively. The data show a large dispersion and the results obtained through these methods differ on average by a factor of 3. We also use the quadratic $M_{\rm SMBH}$-n relation instead of the linear one given by Graham & Driver (2007), and no major differences are observed. This result might reflect the fact that we do not find any correlation between $M_{\rm bulge}$ and n. As can be seen in Figure 6, neither FR I nor FR II bulge luminosities correlate with the concentration index. Note that similar bulge luminosity and n distributions for FR Is and FR IIs also imply similar $M_{\rm SMBH}$ distributions for both subsamples.

8. CONCLUSIONS

We have analyzed the infrared photometric parameters of 82 galaxies belonging to the 3CR catalog. From the morphological point of view most of these galaxies are not yet classified, and classified galaxies are mostly ellipticals. Nevertheless, we find that only 43 (52%) of the galaxies have a single-component luminosity profile. The remaining 39 galaxies (48%) need a second component with $\beta = 1$, suggesting the idea that these galaxies have an exponential disk. However, we cannot confirm this possibility without additional kinematical information. When FR Is and FR IIs are differentiated we find the following results:

1. Forty-five percent of FR Is show a single luminosity profile while for FR IIs this percentage is 55%. Reciprocally, 56% of FR I galaxies show bulge+exponential type profiles compared to 44% of FR II galaxies.
2. Analysis of the photometric parameters of both FR I and FR II galaxies indicates that they have similar bulge and envelope magnitudes. Moreover, FR I and FR 2 bulges follow similar Kormendy relations. Even so, if we consider the exponential component, we have that FR Is have (*a*) dimmer central surface magnitudes and (*b*) much larger scale lengths than FR IIs. K-S tests applied to the μ_0 and r_0 distributions confirm these results at a >98% confidence level.

We also choose another classification scheme, one that relies on the spectroscopic properties and is more likely to reflect the physical properties of the sources. We divided the sample galaxies into four groups, FR Is, LEGs, HEGs, and QSOs. The results of the analysis were similar to those obtained with the previous classification. FR I galaxies show again for the exponential component dimmer central surface magnitudes and much larger scale lengths than the rest of the selected classes (>98% confidence level). However, we also find that these differences are less conspicuous when FR Is are compared to LEGs.

Black hole masses were also calculated using two different methods, using the concentration index and the bulge total luminosity. The results show great dispersion, and black hole masses obtained through $L_{\rm bulge}$ are on average a factor of 3 higher than those obtained through β. This result is not surprising since we did not find a clear correlation between $L_{\rm bulge}$ and β.

Summarizing, past results on the host galaxies of FR I and FR II sources gave confusing results on their properties and morphologies. Thanks to the *HST* NICMOS data we can now probe deeply into the nuclear regions of the hosts and we can clearly distinguish the contributions from the host galaxies and the nuclear sources. We show that the host galaxies have very similar bulge properties while there seems to be a real difference in the

properties or presence of disklike components. These results indicate that the formation histories of the different classes of radio galaxies may be significantly different.

We would like to thank the anonymous referee for a comprehensive report that allowed us to improve this paper. Support for this work was provided by the National Science Foundation through grant N1183 from the Association of Universities for Research in Astronomy, Inc., under NSF cooperative agreement AST 01-32798. D. M. is supported by NASA LTSA NNG04GE12G. This research has made use of the NASA Astrophysics Data System Bibliographic services. This research also made use made use of the NASA/IPAC Extragalactic Database (NED), which is operated by the Jet Propulsion Laboratory, California Institute of Technology, under contract with the National Aeronautics and Space Administration.

REFERENCES

Aller, M. C., & Richstone, D. 2002, AJ, 124, 3035
Bagget, W. E., Bagget, S. M., & Anderson, K. S. J. 1998, AJ, 116, 1626
Bennett, A. S. 1962a, MmRAS, 68, 163
———. 1962b, MNRAS, 125, 75
Blandford, R. D. 2000, Philos. Trans. R. Soc. London A, 358, 811
Brown, R. J. N., et al. 2003, MNRAS, 341, 747
Byum, Y. I., & Freeman, K. 1995, ApJ, 448, 563
Chiaberge, M., Capetti, A., & Celotti, A. 2002, A&A, 394, 791
Coenda, V., Donzelli, C. J., Muriel, H., Quintana, H., Infante, L., and Garcia Lambas, D. 2005, AJ, 129, 1237
de Jong, R. S., Simard, L., Davies, R. L., Saglia, R. P., Burstein, D., Colless, M., McMahan, R., & Wegner, G. 2004, MNRAS, 355, 1155
de Vaucouleurs, G. 1948, Ann. d'Astrophys., 11, 247
Dickinson, M. E., et al. 2002, *HST* NICMOS Data Handbook, Version 5.0, ed. B. Mobasher (Baltimore: STScI)
Djorgovski, S., & Davis, M. 1987, ApJ, 313, 59
Dressler, A., Lynden-Bell, D., Burstein, D., Davies, R. L., Faber, S. M., Terlevich, R., & Wegner, G. 1987, ApJ, 313, 42
Dunlop, J. S., McLure, R. J., Kukula, M. J., Baum, S. A., O'Dea, C. P., & Hughes, D. H. 2003, MNRAS, 340, 1095
Fanaroff, B. L., & Riley, J. M. 1974, MNRAS, 167, 31P
Ferrarese, L., & Merrit, D. 2000, ApJ, 539, L9
Freeman, K. C. 1970, ApJ, 160, 811
Gonzalez-Serrano, J. I., Carballo, R., & Perez-Fournon, I. 1993, AJ, 105, 1710
Graham, A. W., & Driver, S. P. 2007, ApJ, 655, 77
Graham, A. W., Erwin, P., Caon, N., & Trujillo, I. 2003, Rev. Mex. AA Ser. Conf., 17, 196
Hardcastle, M. J., & Worrall, D. M. 2000, MNRAS, 319, 562
Héraudeau, P., & Simien, F. 1996, A&AS, 118, 111
Hine, R. G., & Longair, M. S. 1979, MNRAS, 188, 111
Jackson, N., & Rawlings, S. 1997, MNRAS, 286, 241
Jedrzejewski, R. 1987, MNRAS, 226, 747
Kauffmann, G., & Haehnelt, M. 2000, MNRAS, 311, 576
Kent, S. M. 1985, ApJS, 59, 115
Koekemoer, A. M., Fruchter, A. S., Hook, R. N., & Hack, W. 2002, in The 2002, *HST* Calibration Workshop: Hubble after the Installation of the ACS and the NICMOS Cooling System, ed. S. Arribas, A. Koekemoer, & B. Whitmore (Baltimore: STScI), 339
Kormendy, J. 1977, ApJ, 218, 333
Kormendy, J., & Kennicutt, R. C., Jr. 2004, ARA&A, 42, 603
Kormendy, J., & Richstone, D. 1995, ARA&A, 33, 581
Krist, J. 1993, in ASP Conf. Ser. 52, Astronomical Data Analysis Software and Systems II, ed. R. J. Hanisch, R. J. V. Brissenden, & J. Barnes (San Francisco: ASP), 536
Laing, R. A. 1994, in ASP Conf. Ser. 54, The First Stromlo Symposium: The Physics of Active Galaxies, ed. G. V. Bicknell, M. A. Dopita, & P. J. Quinn (San Francisco: ASP), 227
Madrid, J. P., et al. 2006, ApJS, 164, 307
Magorrian, J., et al. 1998, AJ, 115, 2285
Marchesini, D., Capetti, A., & Celotti, A. 2005, A&A, 433, 841
Marconi, A., & Hunt, L. K. 2003, ApJ, 589, L21
Möllenhoff, C., & Heidt, J. 2001, A&A, 368, 16 (MH01)
Noll, K., et al. 2004, NICMOS Instrument Handbook, Version 7.0 (Baltimore: STScI)
Pahre, M. A. 1999, ApJS, 124, 127
Ryden, S. 1992, ApJ, 396, 445
Sandage, A. R., Freeman, K. C., & Stokes, N. R. 1970, ApJ, 160, 831
Schombert, J. M., & Bothun, G. D. 1987, AJ, 93, 60
Seigar, M. S., Graham, A. W., & Jerjen, H. 2007, MNRAS, 378, 1575
Sérsic, J. L. 1968, Atlas de Galaxias Australes (Córdoba: Obs. Astron.)
Spinrad, H., Marr, J., Aguilar, L., & Djorgovski, S. 1985, PASP, 97, 932
Suchkov, A., & Krist, J. 1998, Instrument Science Report NICMOS 98-018 (Baltimore: STScI)
Tremaine, S., et al. 2002, ApJ, 574, 740
Tully, R. B., & Fisher, J. R. 1977, A&A, 54, 661
Urry, C. M., & Padovani, P. 1995, PASP, 107, 803
Veilleux, S., et al. 2006, ApJ, 643, 707
Zirbel, E. L. 1996a, ApJ, 473, 144
———. 1996b, ApJ, 473, 713
———. 1997, ApJ, 476, 489